ABSTRACT

Title of dissertation: INTERACTION OF INTENSE LASER PULSES WITH GAS FOR TWO-COLOR THZ GENERATION AND REMOTE MAGNETOMETRY

Luke A. Johnson, Doctor of Philosophy, 2014

Dissertation directed by: Professor Thomas Antonsen
Departments of Physics and Electrical & Computer Engineering
Professor Phillip Sprangle
Departments of Physics and Electrical & Computer Engineering

The interaction of intense laser pulses with atmospheric gases is studied in two contexts: (i) the generation of broadband terahertz radiation via two-color photoionization currents in nitrogen, and (ii) the generation of an electromagnetic wakefield by the induced magnetization currents of oxygen.

(i) A laser pulse propagation simulation code was developed to investigate the radiation patterns from two-color THz generation in nitrogen. Understanding the mechanism for conical, two-color THz furthers the development of broadband THz sources. Two-color photoionization produces a cycle-averaged current driving broadband, conically emitted THz radiation. The THz emission angle is found to be determined by an optical Cherenkov effect, occurring when the front velocity of the ionization induced current source is greater than the THz phase velocity.

(ii) A laser pulse propagating in the atmosphere is capable of exciting a mag-

netic dipole transition in molecular oxygen. The resulting transient current creates a co-propagating electromagnetic field behind the laser pulse, i.e. the wakefield, which has a rotated polarization that depends on the background magnetic field. This effect is analyzed to determine it's suitability for remote atmospheric magnetometry for the detection of underwater and underground objects. In the proposed approach, Kerr self-focusing is used to bring a polarized, high-intensity, laser pulse to focus at a remote detection site where the laser pulse induces a ringing in the oxygen magnetization.The detection signature for underwater and underground objects is the change in the wakefield polarization between different measurement locations. The magnetic dipole transition line that is considered is the $b^1\Sigma_g^+ - X^3\Sigma_g^-$ transition band of oxygen near 762 nm.

INTERACTION OF INTENSE LASER PULSES WITH GAS FOR TWO-COLOR THZ GENERATION AND REMOTE MAGNETOMETRY

by

Luke A. Johnson

Dissertation submitted to the Faculty of the Graduate School of the
University of Maryland, College Park in partial fulfillment
of the requirements for the degree of
Doctor of Philosophy
2014

Advisory Committee:
Professor Thomas Antonsen, Chair/Advisor
Professor Phillip Sprangle
Professor Ki-yong Kim
Professor Adil Hassam
Professor Edward Ott

Table of Contents

List of Figures

Chapter 1: Introduction

The propagation of intense laser pulses through gases and plasma is of significant scientific and practical interest. Applications include; compact sources for 1 GeV electrons from laser wakefield acceleration [1], generation of ultraviolet and x-ray radiation via high harmonic generation [2], laser generated plasma columns for directing electrostatic discharges [3], and remote sensing via laser induced breakdown spectroscopy [4]. But each application requires understanding the interplay of many physical processes, such as the nonlinear response to the gas specie's polarization in the presence of the laser electric field. For a single gas specie, such as molecular nitrogen, the nonlinear response can be divided into a number of separate effects such as the instantaneous response of the bound electron cloud, the delayed rotational response of the molecule, and the production of plasma via photoionization. Each process can couple back to the fields and modify the laser pulse as it propagates, generate new frequencies of electromagnetic radiation, or accelerate charged particles. Consequently, intense laser-gas interactions have proved to be an interesting and fruitful area of research.

This thesis will explore two phenomena associated with laser-gas interaction: the generation of broadband terahertz radiation via two-color photoionization cur-

rents in nitrogen, and the generation of an electromagnetic wakefield by the induced magnetization currents of oxygen.

1.1 Two-Color THz generation

Electromagnetic THz radiation has a flexible definition in the literature. The name alone suggests that it should refer to frequencies of electromagnetic radiation on the order of 1 THz. But the "THz gap," the range of frequencies in the electromagnetic spectrum that lacks sources and detectors, is often referred to as covering from 0.3 to 20 THz [5]. The use of THz as a descriptor is relaxed further when discussing broadband THz radiation where the pulse bandwidth can reach 75 THz which is well into the mid-infrared [5, 6]. In this work, THz radiation will typically refer to broadband THz pulses.

A number of different mechanisms can be responsible for the generation of THz radiation. However, the mechanisms share a common feature: charged particles (typically electrons) oscillating at THz frequencies. For example, in an accelerator, coherent synchrotron radiation will produce single-cycle THz pulses from electron bunches with sub-picosecond density modulations. At Brookhaven Lab, a ~ 100 μJ single cycle THz pulses with peak fields of ~ 3 MV/cm was generated [5]. A second example involves electro-optic crystals, such as $LiTaO_3$ or $LiNbO_3$, which produce a nonlinear polarization that depends on the electric field squared. This allows for rectification of femtosecond laser pulses generating THz radiation [7, 8]. Another mechanism for THz generation uses the electrostatic fields of a laser-accelerated,

sub-picosecond electron bunch to drive transition radiation at a plasma-vacuum interface [9].

Hamster *et al.* [10] made the first observation of THz radiation from a laser generated plasma. An intense laser pulse (10^{18} to 10^{19} W/cm^2) was focused on gas targets. Field ionization generated a plasma and then, on the timescale of the laser pulse (100 fs), the electrons were driven away from the ions via the pondermotive force. This pondermotive current drove the THz radiation. The emitted radiation had an energy of ~ 0.1 nJ and was centered at a few THz.

The first observation of THz generation due to an intense laser pulse composed of a fundamental frequency and its harmonic, a "two-color pulse," was made by Cook *et al.* [11]. Cook *et al.* observed ~ 5 pJ THz pulses with peak fields of ~ 2 kV/cm which was comparable to optical rectification in electro-optic crystals. The THz generation mechanism was attributed to an unknown four-wave mixing process. Interestingly, several possible THz generation mechanisms were discussed in Ref. [11]. The first being the nonlinear response of the bound electrons. But, the THz energy scaling did not match the expected dependence on the intensities of the two colors. The second possibility proposed by Cook *et al.* was that a field-ionization process was occurring, but they lacked the ability to scan a large enough range of laser intensities to investigate this effect. Another unexplored possibility was that excited or Rydberg states where being created and they were contributing to an enhanced nonlinear susceptibility. Later experimental work also observed that the THz yields were two orders of magnitude larger than what would be expected based on the nonlinear susceptibility of air [12]. Additionally, these works found

that the THz energy scaling was observed to follow $U_{\mathrm{THz}} \propto I_2 I_1^2$ (where I_1 is the fundamental intensity and I_2 is the second harmonic intensity) which is suggestive of an four-wave mixing process, but this scaling only occurred when the laser intensity was sufficiently high to field ionize the gas [12–14]. This firmly connected the THz generation with plasma formation, but the mechanism remained unknown and continued to be described in the context of four-wave mixing.

It was proposed that the THz generation mechanism involves the generation of a current, called a photocurrent, on the timescale of the laser pulse by electrons that are field ionized [15]. The previously observed sinusoidal dependence of the THz yield with propagation distance is consistent with both the photocurrent [15] and four-wave mixing models [11, 12]. But in Ref. [15], the oscillating behavior in the THz yield was shown to indicate that the THz yield is minimal when the field peaks of the two colors are coincident. This result is inconsistent with the four-wave mixing model. Additionally, a preformed plasma was shown to reduce the THz yield [15]. This bolstered the argument that THz generation is not due to a nonlinear susceptibility, but rather, due to ionizing the gas. Later work provided the theoretical underpinning for the two-color photocurrent model and is the basis of the current understanding of the fundamental mechanism for two-color THz generation [6].

Understanding the mechanism of two-color THz, as explained by Kim *et al.* [15], is important for understanding why the THz is emitted with a conical radiation profile. A typical experimental setup is as follows [15]. A femtosecond laser pulse with millijoule energies is focused into a nitrogen gas cell. As the fundamental

pulse propagates, it passes through a beta barium borate (BBO) crystal, and a copropagating second-harmonic (400 nm) pulse is generated. The fundamental and second-harmonic pulses will be referred to as the "pump pulses." The pump pulses largely overlap both spatially and temporally as they approach their common focal point. When they reach sufficient intensity, they weakly ionize the gas and generate THz radiation.

The THz radiation is generated when electrons, produced by ionization, create a cycle-averaged current on the time scale of the pump-pulses' envelope (25 fs). Atoms are preferentially ionized at temporal peaks in the laser field and the resulting electrons are born with essentially zero velocity. This is illustrated by the location of the peak ionization rate and the initial slope of the electron trajectories in Fig. 1.1. In a single-color pulse, as shown in Fig.1.1(a), electrons ionized on either side of the peak field acquire drift velocities in opposite directions. The ensemble average drift velocity of the resulting electrons is zero, and therefore no macroscopic, cycle-averaged current is produced. However, when two colors are present with the appropriate relative phase, for example in Fig. 1.1(c), they interfere, and electrons acquire a macroscopic, cycle-averaged current. The cycle-averaged current builds up on the time scale of the pump-pulses' duration and drives the THz fields.

Experimentally, the THz radiation is observed to have a conical radiation profile relative to the laser pulse axis [16]. An example of a slice of the conical THz profile is seen in Fig. 1.2(a) [17]. The conical THz was previously explained by off-axis phase matching from a line source of periodic THz emitters [16]. It was proposed that the THz line source was created by the phase-velocity mismatch between the

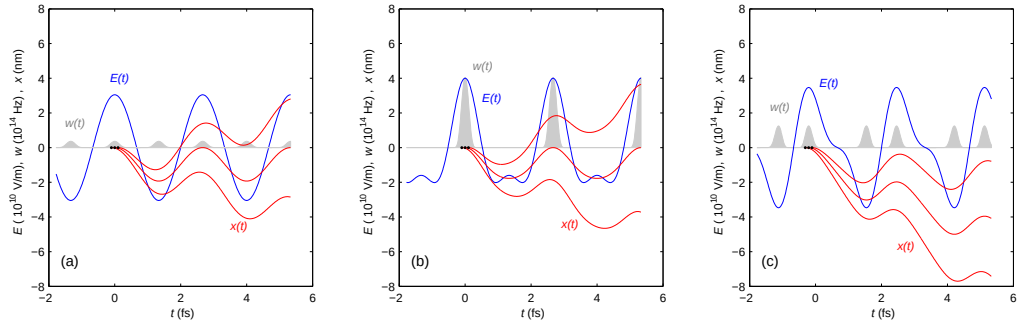

Figure 1.1: Example electron trajectories (red) are shown beside the electric field (blue) and ionization rate (grey) as a function of time in three different scenarios; (a) single-color field, (b) two-color field with relative phase $\theta = 0$, and (c) two-color field with relative phase $\theta = \pi/2$. In can been seen from the net downward displacement of the electrons in (c) that the ensemble of electrons will pick up a net drift velocity for a two-color field with $\theta = \pi/2$. The axes units are as follows; 10^{-9} m for electron trajectories (red), 10^{10} V/m for electric field (blue), 10^{14} Hz for ionization rate (grey), and 10^{-15} s for time. See references [6, 15] for more details.

800 nm and 400 nm pulses and the resulting oscillation of the photoionization current with propagation distance.

To investigate this phenomenon we developed a two-dimensional, nonlinear, spectral, electromagnetic code that models the propagation of radiation from THz to ultraviolet frequencies. Few-cycle THz pulses are observed in the simulations that propagate at an angle, $\phi \approx 1^\circ$, above and below the optical axis, as seen in Fig. 1.2(b). We identified the mechanism responsible for two-color conical THz radiation to be a Cherenkov effect. In this model the cycle-averaged current, created by the pump pulses, moves faster than the THz propagation velocity, thereby generating conical radiation. Additionally, the two-color Cherenkov model was extended to capture the behavior of the "oscillating current" model introduced by You *et al.* [16]. In this way both effects can be seen as different limits of one model. However, the spatially varying currents necessary for the "oscillating current" model were not

observed in simulations implying that the optical Cherenkov mechanism is dominant. [18]. It is noted that optical Cherenkov is a common mechanism to achieve the necessary phase matching for the generation of THz radiation in electro-optic crystals by the nonlinear optics community [7].

There are two THz generation mechanisms that appear similar to that in this work but are in fact different. The first is that of D'Amico *et al.* [19, 20], observed conical THz radiation and interpreted it as a form of the Cherenkov effect. However, D'Amico *et al.* used a single-color laser pulse to drive a collisionally-damped, few-cycle plasma oscillation via the pondermotive force. Whereas, the two-color Cherenkov mechanism requires a two-color laser pulse to drive photocurrents and operates at intensities for which the pondermotive force is negligible. The second was proposed by Peñano *et al.* [21] and involves the four-wave mixing of a two-color laser pulse in a collisional, preionized plasma. While this mechanism does require a two-color laser pulse, it does not produce conical THz via a Cherenkov process. Additionally, it relies on the pondermotive force which is not significant for intensities considered in our work.

1.2 Electromagnetic Wakefields from Oxygen Magnetization

A high-intensity pump laser pulse can be employed to drive a magnetization current in molecular oxygen. This is possible because oxygen's ground state has a total spin 1 and therefore an oscillating magnetic field can drive an oscillation in oxygen's magnetic moment. After the intense laser pulse has passed, the magne-

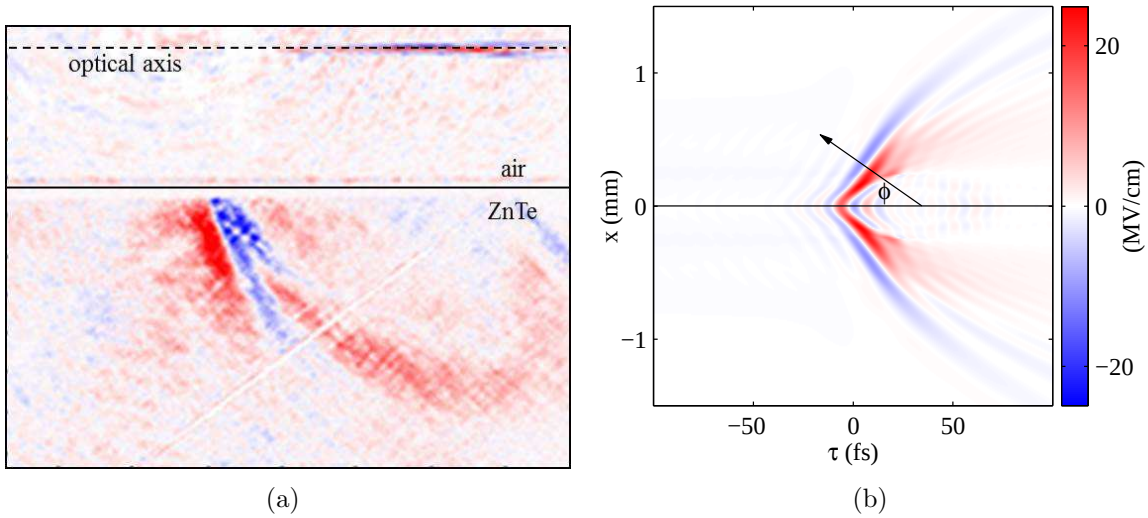

Figure 1.2: (a) Experimental and (b) simulation examples of conical few-cycle THz pulses. The experimental figure shows a snapshot of the spatial profile of THz pulse inside a ZnTe crystal. The simulation shows the THz pulse directly after its creation as a function of transverse space and time in the light frame. There is a direct correspondence between the temporal axis and the optical axis.

tization current from the oxygen will be left ringing at approximately the pump frequency and will slowly damp away due to collisions with atmospheric molecules. This forms an electromagnetic wakefield that trails behind the laser pulse. In the presence of a static background magnetic field, the Zeeman effect causes a splitting in the ground state energy levels. This energy level splitting means that polarization of the magnetization wakefield will rotate around the optical access in proportion to the magnetic field strength.

This mechanism can, in principle, provide a means to remotely measure variations in the earth's magnetic field in atmospheric conditions. For a number of magnetic anomaly detection (MAD) applications, such as detection of nuclear submarines, 10 μG magnetic field variations must be detected at standoff distances of

approximately one kilometer from the sensor [22]. Other applications include detection of unexploded ordinance and underwater mines.

The propagation of the high-intensity pump laser pulse to remote detection sites is considered. We show that high laser intensities (below $10^{12}\,\mathrm{W/cm^2}$ to avoid photoionization processes) can be propagated to remote locations due to the self focusing optical Kerr effect. We consider the magnetization currents that are left ringing behind the pump pulse and the resulting co-propagating electromagnetic field. This field is referred to as the wakefield and it undergoes polarization rotation due to the Zeeman splitting of oxygen's ground state. The magnetic field variation is detected by measuring the wakefield's polarization.

Molecular oxygen's paramagnetic response is due to two unpaired valance electrons. The ground state of oxygen $X^3\Sigma_g^-$, commonly referred to as "triplet oxygen," has total angular momentum $J = 1$, total spin $S = 1$, and three degenerate sublevels. The excited upper state being considered is denoted by $b^1\Sigma_g^+$. It has $J = 0$ and is a spin singlet state $S = 0$ with only one sublevel. The upper state can undergo three radiative transitions, $b^1\Sigma_g^+ \rightarrow X^3\Sigma_g^-(m = \pm 1)$, $b^1\Sigma_g^+ \rightarrow X^3\Sigma_g^-(m = 0)$, but the latter is insignificant because it is an electric quadruple transition. The O_2 transition line being considered is the $b^1\Sigma_g^+ - X^3\Sigma_g^-$ transition band of oxygen near 762 nm. In the low intensity, long laser pulse, regime, this transition has been investigated theoretically [23, 24] and experimentally [25] and is a prominent feature of air glow.

A major challenge for this, as well as any remote atmospheric optical magnetometry concept, is collisional dephasing (elastic collisions) of the transitions. The

elastic molecular collision frequency, at standard temperature and pressure (STP), is $\gamma_c = N_{\text{air}}\sigma v_{th} = 3.5 \times 10^9\,\text{s}^{-1}$, where σ is the molecular cross section and v_{th} is the thermal velocity [25]. The Larmor frequency in the earth's magnetic field is $\Omega_0 = qB_0/(2mc) \approx 4.5 \times 10^6\,\text{rad/s}$ ($\hbar\Omega_0 = 3 \times 10^{-9}\,\text{eV}$), where m and q are the electron mass and charge and c is the speed of light, is much smaller than the collision frequency. Since the dephasing frequency is far greater than the Larmor frequency, the parameters are somewhat restrictive for remote atmospheric magnetometry. However, rotational magnetometry experiments based on molecular oxygen at STP and magnetic fields of $\sim 10\,\text{G}$ have shown measurable linear Faraday rotational effects [25].

Previous theoretical work [24] revealed major issues with atmospheric magnetic field measurements using oxygen, these include: (1) extremely low photon absorption cross sections, (2) a broad magnetic resonance linewidth due to collisions, and (3) quenching of excited-state fluorescence. These issues largely stem from oxygen's small magnetic dipole moment and large collision rate. In our work, however, the wakefield's polarization rotation is the magnetic signature and the laser pulse intensities are approximately six orders of magnitude larger.

Chapter 2: Two-color THz Generation

2.1 Overview

Ultrashort, ultraintense laser pulses propagating through and ionizing gases have produced intense pulses of THz radiation. The large electric and magnetic fields of these pulses are potentially useful for a variety of applications [5]. For example, intense magnetic fields (≈ 1 T) with subpicosecond duration can be used for coherent control of the spin degree of freedom, in spintronic systems, exciting and deexciting spin waves [26]. In molecular spectroscopy, the high electric fields (≈ 1 MV/cm) of THz pulses can be used to orient molecules for transient birefringence and free induction decay measurements [27]. Using ultrashort laser pulses to generate THz via air breakdown may provide a scalable, compact source of few-cycle THz pulses when compared to modern accelerators [5]. Scaling to higher energies is possible because field-induced breakdown of the medium is a feature, not a limitation. In addition, the compact nature of these sources and their ability to use air as a generation medium potentially allows for standoff capabilities [28]. Generating the THz close to its target decreases the distance over which the THz must propagate, limiting atmospheric absorption [29]. Developing such a THz source will require an understanding of the competing nonlinear interactions in atmospheric gases.

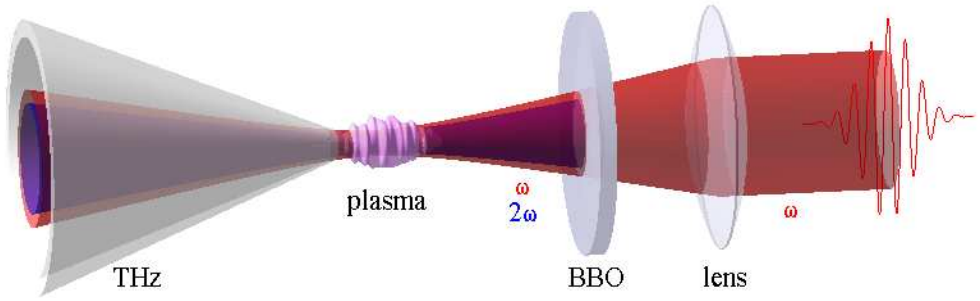

Figure 2.1: This is a schematic of the experimental setup that is being simulated. The simulation domain includes everything to the left of the BBO crystal. As the two-color pulse (red and blue) approaches focus, it ionizes the gas and generates a plasma. The THz radiation (gray) exits the other side of the plasma as a cone [16].

Cook *et al.* [11] reported using an ultrashort laser pulse consisting of two colors, a fundamental (800 nm) and its second harmonic (400 nm), to produce approximately 5 pJ of THz radiation between 0 and 5 THz. Recent experiments have been able to reach 7 μJ for frequencies below 10 THz [30]. The generation mechanism was originally explained as optical rectification via an unspecified third-order nonlinearity. In 2007, Kim *et al.* [6,15] described the process as tunneling ionization that induces transverse currents on the time scale of the laser pulse envelope (50 fs). Recent three-dimensional simulations by Bergé *et al.* [31] have shown that the bulk of the THz generation in argon, which has a similar ionization potential to N_2, can be explained by this mechanism. One feature in recent experiments [16] is that the THz radiation is observed to emerge in the forward direction (parallel to the axis of the two laser pulses) in a cone with angle roughly 4° to 7° with respect to the optical axis. In this chapter we will explore the mechanism contributing to this effect.

We are interested in modeling an experimental setup similar to that of You *et al.* [16], as shown in Fig. 2.1. In our setup, an ultrashort pulse with a wavelength

of 800 nm, duration of 25 fs, and energy of 0.8 mJ is focused into a nitrogen gas cell. As the fundamental pulse propagates, it passes through a beta barium borate (BBO) crystal, and a copropagating second-harmonic (400 nm) pulse is generated. The fundamental and second-harmonic pulses will be referred to together as the "pump pulses." The pump pulses largely overlap both spatially and temporally as they approach their common focal point. When they reach sufficient intensity, they weakly ionize the gas and generate THz radiation.

The THz radiation is generated when the electrons produced by ionization create a cycle-averaged current on the time scale of the pump-pulses' envelope. Atoms are preferentially ionized at temporal peaks in the laser field and the resulting electrons are born with essentially zero velocity. In a single-color pulse, electrons ionized on either side of the peak field acquire drift velocities in opposite directions. The resulting electrons have no ensemble-averaged drift velocity, and therefore no macroscopic, cycle-averaged current. However, when two colors are present with the appropriate relative phase, they interfere, and electrons acquire a macroscopic, cycle-averaged current. The cycle-averaged current builds up on the time scale of the pump-pulses' duration and drives the THz fields. This two-color THz generation mechanism is sometimes couched as a four-wave mixing process, but, strictly speaking, it is not due to a third-order nonlinearity.

There are other mechanisms which can modify the two-color, cycle-averaged current or even produce a cycle-averaged current in the absence of the second color. The envelope in few-cycle, single-color laser pulses varies fast enough that a cycle-averaged current on the time scale of the envelope can be created [32]. This cur-

rent can drive broadband THz radiation similar to the two-color mechanism. For laser pulses intense enough to deplete the neutral gas, a cycle-averaged current can be formed. This occurs because, during a half cycle, there are more neutral gas molecules to ionize on the rise to the peak field than on the decent. The optimal phase for THz generation in intense, two-color pulses can be modified by this effect [33]. Both effects are included in our model, but are not significant for the parameters we consider. A third effect related to the time variation of the envelope of an elliptically polarized laser pulse is not included in our study, which focuses on linearly polarized fields.

We observe in simulations few-cycle THz pulses that propagate at an angle, $\phi \approx 1°$, above and below the optical axis. This can be explained with an optical Cherenkov model, where the cycle-averaged current, created by the pump pulses, moves faster than the THz propagation velocity. Optical Cherenkov is a common mechanism for generating THz radiation in electro-optic crystals by the nonlinear optics community [7]. We will also discuss a unification of our Cherenkov model with the "oscillating current" model introduced by You *et al.* [16]. In this way both effects can be seen as different limits of one model. D'Amico *et al.* [20] observed conical THz and it was interpreted as a transition-Cherenkov effect, i.e., a single-color optical pulse drives a collisional-damped, few-cycle plasma oscillation via the pondermotive force. The plasma wake following the drive laser emits THz radiation as if it were a dipole aligned with the optical axis, traveling at the speed of the optical pulse. This differs from our mechanism in two ways: The cycle-averaged current is transverse to the direction of propagation and is not driven by the pondermotive

force.

The organization of this chapter is as follows: First we will describe the components of our propagation and material response models. During this we will discuss the necessity of including each physical phenomena in our model for studying THz generation. Finally, we will describe the Cherenkov model, its connection to the oscillating current model, and analyze our simulation results.

2.2 Model

2.2.1 Unidirectional Pulse Propagation Model

The optical and THz pulses of interest propagate predominately in the forward direction [34], justifying the use of the unidirectional pulse propagation equation (UPPE) [35], where the main assumption is that the backward propagating fields do not contribute to the nonlinear response of the medium. The UPPE is amenable to pseudospectral methods which reduce the electromagnetic propagation equation to a set of coupled ordinary differential equations for the field's spectral components. Since the fields are propagated in the spectral domain, the UPPE captures linear dispersion to all orders, allowing treatment of broadband, multicolor pulses.

The electric field's spectral components $\widehat{E} = \widehat{E}(k_x, z, \omega)$ are propagated along z according to

$$\partial_z \widehat{E} = -i \left[k_z - \frac{\omega}{v_w} \right] \widehat{E} + \frac{\widehat{S}}{-2ik_z}, \tag{2.1}$$

where

$$\widehat{S}(k_x, z, \omega) = -\mu_0 \omega^2 \widehat{P}^{(\mathrm{NL,gas})} + \mu_0 \frac{\widehat{\partial J}}{\partial \tau} + i\mu_0 \omega \widehat{J_{\mathrm{loss}}}. \tag{2.2}$$

The variables ω and k_x are Fourier conjugates to the time coordinate in a window moving with velocity v_w, $\tau = t - z/v_w$, and the transverse dimension, x, respectively. The medium's nonlinear response to the field, $S(x, z, \tau)$, is calculated in the (x, τ) domain and then transformed to the spectral domain, $\widehat{S} = \widehat{S}(k_x, z, \omega)$, to drive the fields. The z component of the wave number, $k_z = k_z(k_x, \omega)$, depends on the frequency and transverse wave number, and includes the linear response of the gas through the refractive index, $n(\omega)$. Specifically, $k_z(k_x, \omega) = \sqrt{\omega^2 n(\omega)^2/c^2 - k_x^2}$. The propagation constant in Eq. (2.1), $k_z - \omega/v_w$, reflects the shift in the z component of the wave number due to the moving window. The nonlinear response of the medium can be decomposed into a bound nonlinear response of the neutral gas $\widehat{P}^{(\mathrm{NL,gas})}$, the free electron response $\widehat{\partial_\tau J}$, and an effective current to deplete the field energy during ionization, $\widehat{J_{\mathrm{loss}}}$.

2.2.2 Material Response of Molecular Nitrogen

The frequency dependent refractive index for molecular nitrogen, $n(\omega) = 1 + \delta n_{\mathrm{PK}}(\omega)$, in the range $106 - 549\,\mathrm{THz}$ $(2.8 - 0.5\,\mu\mathrm{m})$ is given by an equation fit to experimental data and is provided by Peck and Khanna [36],

$$10^8 \delta n_{\mathrm{PK}}(\omega) = 6497.378 + \frac{3073864.9\ \ \mu\mathrm{m}^{-2}}{144\ \ \mu\mathrm{m}^{-2} - (\omega/2\pi c)^2}. \tag{2.3}$$

For frequencies below 106 THz, the index is found by extrapolating Eq. (2.3). Recent experiments in air [37] have indicated $n_{\text{air}} - 1 \approx 1.7 \times 10^{-4}$ at THz frequencies, which is similar to the zero frequency limit of Eq. (2.3), $n(0) - 1 = 2.78 \times 10^{-4}$. By extrapolating Eq. (2.3), the detailed structure in the refractive index due to vibrational and rotational excitations of N_2 is not included.

The nonlinear bound response of neutral N_2 is captured in the nonlinear polarization density, $\widehat{P}^{(\text{NL,gas})}$, and is calculated in the (x, τ) domain using

$$P^{(\text{NL,gas})} = \frac{4}{3} c \epsilon_0^2 n_2^{(\text{inst})} E^3 + \epsilon_0 n_0 \Delta\alpha Q E. \tag{2.4}$$

Here, two third-order nonlinear processes contribute to the polarization density: an instantaneous electronic response and a delayed rotational response, the first and second terms of Eq. (2.4), respectively. In a classical picture of the instantaneous nonlinear bound response, the laser field strongly drives bound electrons and they experience the anharmonicity of the binding potential. Because gases are isotropic on macroscopic scales, the lowest-order nonlinear polarization to manifest itself at macroscopic scales is proportional to E^3, instead of E^2. We use $n_2^{(\text{inst})} = 7.4 \times 10^{-20}$ cm^2/W at a N_2 density of $n_0 = 2.5 \times 10^{19}$ cm^{-3} [38]. The delayed response arises because the laser field applies a torque to the N_2 molecules due to the anisotropy in their linear polarizability, $\Delta\alpha = \alpha_{\parallel} - \alpha_{\perp} = 6.7 \times 10^{-25}$ cm^3, where $\alpha_{\parallel,\perp}$ are the linear polarizabilities parallel and perpendicular to the molecular axis, respectively. A simple model for the molecular alignment of the gas,

$Q = Q(x, z, \tau)$, is to treat it as a driven, damped, harmonic oscillator:

$$\frac{\partial^2 Q}{\partial \tau^2} + 2\nu \frac{\partial Q}{\partial \tau} + \Omega^2 Q = 2\Omega^2 n_2^{(\text{align})} \epsilon_0 c E(\tau)^2. \tag{2.5}$$

The oscillator parameters $\nu = 9.6\,\text{THz}$, $\Omega = 18\,\text{THz}$, $n_2^{(\text{align})} = 1.35 \times 10^{-15}\ \text{cm}^2/\text{W}$ are chosen to best match density matrix calculations [39] where the laser pulse duration, ≈ 25 fs, is much shorter than the thermal rotational time scale, $2\pi/\Omega$. These two nonlinear processes result in propagation effects such as spectral broadening, harmonic generation, and self-focusing.

During propagation of high power, ultrashort laser pulses, field ionization is the primary mechanism for free electron generation. This can be modeled with a rate equation for the electron density, $n_e = n_e(x, z, \tau)$, where

$$\frac{\partial n_e}{\partial \tau} = w\,(n_0 - n_e)\,. \tag{2.6}$$

The rate of electron generation is the ionization rate of a single molecule, $w = w[E(x, z, \tau)]$, times the number density of neutral molecules, $n_n = n_0 - n_e$, where n_0 is the initial density of the neutral gas. Here we neglect electron transport, recombination, and attachment; the time scales for these processes are much longer than the pump-pulses' duration [40].

We use a two-color hybrid ionization rate, $w[E]$, which is a fit to a Perelomov, Popov, and Terent'ev (PPT) ionization rate [41] when $w[E]$ is cycle averaged. The ionization rate includes multiphoton ionization (MPI) for the two pump-pulse fre-

quencies and tunneling ionization (TI). MPI is an Nth-order perturbative process in the intensity, where a bound electron escapes from its binding potential by absorbing N photons with energy $\hbar\omega$ and frequency ω. The energy in the N photons must be greater than or equal to the binding energy U_i; $N\hbar\omega \geq U_i$. Tunneling ionization occurs when the instantaneous electric field deforms the binding potential enough to create a classically allowed region outside the atomic or molecular core. With some probability, an electron can tunnel through the barrier between the classically bound and classically free regions, resulting in a free electron. Further details of the two-color hybrid rate and how it was fit to the limiting cases are given in the Appendix.

The free electron current $J = J(x, z, \tau)$ is determined by the electron momentum balance equation,

$$\frac{\partial J}{\partial \tau} = \frac{e^2}{m_e} n_e E - \nu_{en} J. \tag{2.7}$$

It is through this current that the THz will be generated. In Eq. (2.7), the electron density is time dependent due to ionization. There is no momentum source term accompanying the ionization because we assume that new free electrons are born at rest. It can be shown that the solution of this equation for the macroscopic current is equivalent to the single particle picture of Kim *et al.* [6, 42]. We include a fixed collision frequency, $\nu_{ne} = 5\,\mathrm{THz}$, to account for electron-neutral collisions which dominate electron-ion collisions in a weakly ionized gas. The collision frequency of 5 THz is found by approximating the neutral N_2 density as atmospheric density and assuming that the electron's temperature is approximately the quiver energy at field

intensities of $10^{13} - 10^{14}\,\mathrm{W/cm^2}$ [40].

The second source term for the electromagnetic fields [see Eq. (2.2)] is the Fourier transform of the time derivative of the current, $\partial_\tau J$. Care must be exercised in its numerical evaluation. If J is solved for in the time domain and then Fourier transformed, the moving window must extend several collision times, ν_{ne}^{-1}, so that the currents decay to zero. If the domain is too short, the current is finite at the window boundary and its frequency spectrum has an unphysical ω^{-1} dependence. To circumvent this, we Fourier transform $n_e E$, which tends to zero outside of the temporal range of the pump pulses', and compute the Fourier transform of $\partial_\tau J$ via

$$\widehat{\frac{\partial J}{\partial \tau}} = \frac{e^2}{m_e} \frac{\widehat{n_e E}}{1 - i\nu_{en}/\omega}. \tag{2.8}$$

During ionization, the electric field must perform work equal to the ionization potential U_i to liberate each electron. Ionization energy depletion is included by adding an effective current, $J_{\mathrm{loss}} = J_{\mathrm{loss}}(x, z, \tau)$, that accounts for the rate of energy loss: $E J_{\mathrm{loss}} = w[E] n_n U_i$ [43] ,

$$J_{\mathrm{loss}} = \frac{w[E] n_n U_i}{E}. \tag{2.9}$$

To avoid issues when dividing the cycle-averaged contributions of Eq. (2.14) by the instantaneous electric field, the loss current is only evaluated when $|E(t)| > 27$ MV/cm. Below these field strengths, the ionization rate is too small to significantly deplete the pump pulses.

2.3 Conical THz Radiation

We now describe simulation results based on the numerical solution of the model equations introduced in the previous section. The incident electric field is composed of two pulses with central wavelengths $\lambda = 800$ and 400 nm, respectively. The 800 nm pulse has a total energy of 0.7 mJ, a full-width half-maximum duration of 25 fs, and a vacuum spot size of $w_0 = 15.3\,\mu$m. The 400 nm pulse is created experimentally by second-harmonic generation in a BBO crystal. This motivates the 400 nm pulse having a total energy that is 10% of the fundamental pulse, 0.07 mJ, a full-width half-maximum duration that is a factor $\sqrt{2}$ shorter than the fundamental, 18 fs, and a vacuum spot size that is $\sqrt{2}$ smaller than the fundamental, $w_0 = 11\,\mu$m. The pulses are assumed to overlap spatially and temporally with the peak of each pulse colocated 8 cm before the vacuum focus. This is where the BBO crystal ends and the simulation begins. Both colors are initialized with a phase front curvature that is consistent with passing through a lens with focal length and diameter of 15 and 0.5 cm, respectively. The polarization of the pump pulses are assumed to be collinear.

The simulation domain is 6 mm in the transverse spatial dimension, x, and 1 ps in the time domain, τ, with 2^9 and 2^{15} grid points, respectively. The transverse spatial resolution is $\Delta x = 12\,\mu$m. This resolution is sufficient because plasma refraction keeps the pulse from reaching its vacuum spot size. For example, the pump-pulses' time-averaged rms radii is always larger than $100\,\mu$m. At the front of the pulse, where the intensity is lower, the rms radius reaches a minimum of $40\,\mu$m.

The transverse spatial resolutions also resolve the transverse phase variation associated with focusing sufficiently well for the vacuum focal point to remain unchanged. Simulations with double the spatial resolution, $\Delta x = 6\,\mu$m, show convergence of the THz energy and fields. The temporal domain is chosen so as to capture low frequency behavior, $\Delta f = 1$ THz, while having sufficiently small time steps, $\Delta\tau = 0.03$ fs, to resolve ionization bursts and harmonic generation. The pulses propagate 12 cm, with a uniform step size of $\Delta z = 10\,\mu$m. The window velocity, $v_w = 0.99972c$, is comoving with the group velocity of 800 nm in N_2. The background N_2 density is $n_{\text{gas}} = 2.5 \times 10^{19}$ cm^{-3}. The UPPE model, Eq. (2.1), is solved using a second-order predictor-corrector scheme for the nonlinear term, $\widehat{S}$.

The simulation predicts off-axis, broadband, THz radiation as seen in Fig. 2.2. The figure displays the THz electric field as a function of x and τ after propagating to 2 cm before the vacuum focus. To calculate the THz electric field, $\widehat{E}$ has been filtered to remove frequency components with $f > 100$ THz and transformed to the space and time domain. The THz field is a few-cycle pulse that has been created near the axis and is propagating at approximately 1° above and below the propagation axis of the pump pulses. This can be seen from the nulls in the phase (white in the figure) where the fields will propagate perpendicular to the phase front.

2.3.1 Cherenkov Model

The angle of the THz pulse shown in Fig. 2.2 can be explained by an optical Cherenkov effect. As the pump pulses approach focus, their fronts of constant

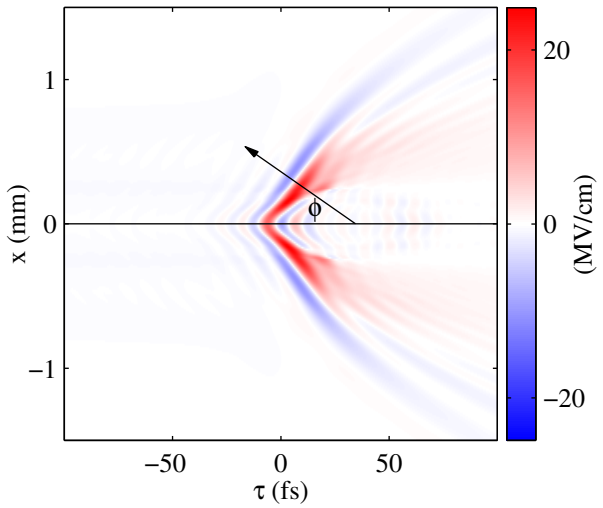

Figure 2.2: The electric field from 0 to 100 THz is shown in the transverse spatial dimension, x, versus a time window that is comoving with the 800 nm pulse, τ. The pulse is propagating from right to left with an off-axis angle ϕ. The electric field at 2 cm before vacuum focus was chosen because most of final THz energy is already in the pulse.

intensity and, through ionization, fronts of constant plasma density move axially faster than the pump-pulses' group velocities. The resulting current drives the THz radiation and travels faster than the THz phase velocity in the medium. This results in a "Cherenkov cone" in which the emitted THz field interferes constructively at the Cherenkov angle ϕ given by $\cos\phi = v_{\mathrm{THz}}(\omega)/v_f$, where v_f is the velocity of the plasma current front and $v_{\mathrm{THz}}(\omega) = c/n(\omega)$ is the THz phase velocity. A schematic of this is shown in Fig. 2.3. The duration of the current approximates the time scale of the pump-pulses' envelope, providing the few-cycle THz phase front observed in Fig. 2.2.

A simple model illustrates this phenomenon. Equations (2.1) and (2.2) can be solved analytically to find the THz field spectrum resulting from a prespecified THz current. We model the current driven by the pump pulses as a localized, on-

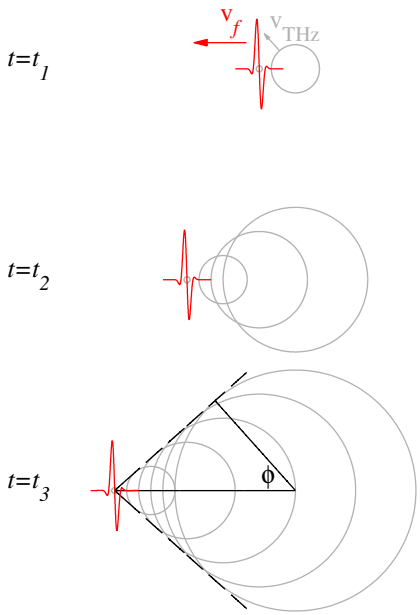

Figure 2.3: The broadband THz frequency current (red) is traveling faster from right to left than the phase velocity of the THz fields (lines of constant phase are shown in gray). Constructive interference can be seen along the front (black dashed) above and below the propagation axis.

axis source with velocity, v_f, $J_p(x,z,t) = I_0\delta(x)\theta(t - z/v_f)$ where I_0 is the current amplitude (A m^{-1} in two dimensions). After the current pulse has propagated a distance, L, the THz spectrum is given by

$$\left|\widehat{E}_{\mathrm{THz}}(k_x, z, \omega)\right|^2 = \frac{I_0^2\mu_0^2}{4k_z^2}\mathrm{sinc}^2\left[\left(\frac{\omega}{v_f} - k_z\right)\frac{L}{2}\right]L^2, \tag{2.10}$$

where $k_z = \sqrt{(\omega n/c)^2 - k_x^2}$. The peaks in the power spectrum occur approximately where the argument of the sinc is zero, reproducing the expression for the Cherenkov angle:

$$\cos\phi = v_{\mathrm{THz}}(\omega)/v_f. \tag{2.11}$$

We note that the THz angle is related to the vector components of the wave number via $k_z = (\omega n/c)\cos\phi$.

This model can be extended to capture a current source with transverse spatial extent or a current source that oscillates along the propagation distance. The latter extension captures the effect on the two-color THz current of phase slippage between the pump pulses due to their phase-velocity difference. This phase slippage was considered in a previous model of off-axis THz emission [16]. You *et al.* [16] treat the THz driving current as a dipole radiator traveling with the laser pulse. The phase of the dipole's oscillation, and hence the emitted radiation, varies along the propagation axis with the relative phase between the pump pulses. In You's model, the group velocity of the laser pulses, the velocity of the driving current, v_f, and the THz phase velocity, v_{THz}, are all set to c. While the model predicts off-axis radiation, the equality of THz and drive velocities precludes Cherenkov radiation. Our model can capture this oscillating current effect if we impose a second spatial variation on the current density, $J_p(x,z,t) = I_0\delta(x)\cos(k_d z)\theta(t-z/v_f)$. In this case the THz spectrum is peaked at angles given by

$$\cos\phi = v_{\mathrm{THz}}/v_f \pm k_d v_{\mathrm{THz}}/\omega, \tag{2.12}$$

where ω is the THz frequency of interest, $k_d = \pi/L_\pi$ is the dephasing wavenumber, and L_π is the distance over which the two colors will phase slip by π.

The dephasing length is inversely proportional to the phase-velocity difference and can be estimated as $L_\pi = (\lambda_0/4)\,|n(\omega_0) - n(2\omega_0)|^{-1}$ [44]. The refractive index is given by $n(\omega) = 1 + \delta n_{\mathrm{gas}}(\omega) + \delta n_{\mathrm{plasma}}(\omega) + \cdots$, where ω could be for either the fundamental, ω_0, or second harmonic, $2\omega_0$. The quantity λ_0 is the wavelength

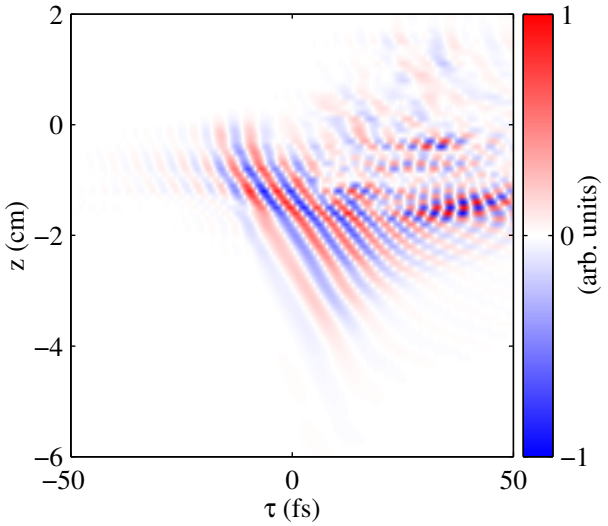

Figure 2.4: The on-axis $\partial_\tau J$ after a low-pass filter with cutoff frequency of 200 THz has been applied.

of the fundamental. From N_2 dispersion alone $L_\pi = 2.7$ cm, but with a plasma density in the range of $10^{16} - 10^{17}$ cm^{-3}, the dephasing length would be $2.1 - 0.7$ cm, respectively. These plasma densities are typical for the region where THz is generated.

Figure 2.4 displays the time derivative of the current density on axis, low-pass filtered to frequencies below 200 THz as a function of z and τ. Most of the THz energy is generated between $z = -4$ and -1 cm, as can be seen in Fig. 2.5. Over this distance, the THz current source has the form of a temporally oscillating signal that moves forward in the frame of the simulation. For comparison, an object moving at the group velocity of 800 nm would trace out a vertical path in (z, τ) domain, while objects moving faster, or slower, follow paths to the left, or right, of vertical respectively. It is the overall forward motion of the THz $\partial_\tau J$ that drives the Cherenkov radiation. The forward motion of the THz current density profile can

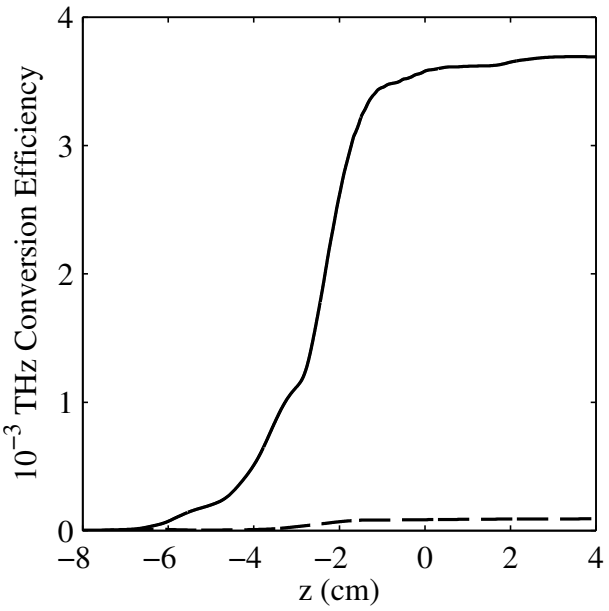

Figure 2.5: The solid line is the energy in the THz from 10 to 100 THz relative to the total initial energy in the pump pulses. The dashed line is for the same simulation parameters, but only the nonlinear gas response was allowed to drive THz radiation.

be attributed to the fact that the pump pulses are converging towards focus. As the pulses converge, their intensity rises, and the time in the pulse envelope when ionization becomes significant moves forward in the plane of Fig. 2.4.

The spatiotemporal form of the current density waveform implied by Fig. 2.4 is that of a few-cycle pulse. The temporal (≈ 10 fs) variations in $\partial_\tau J$ at fixed z are due to a combination of the temporal variation in the pump-pulses' relative phase during the pulse and the frequency upshift of the THz field due to the rising electron density. We note the variations become more rapid with propagation distance. As the pump pulses propagate their relative phase becomes a time varying function due to the rise in electron density during the pulses. The sign of the two-color driven THz current then varies with this relative phase. This variation becomes more rapid with propagation distance. A second contribution to the increase in frequency of the

on-axis $\partial_\tau J$ as a function of propagation distance is the direct spectral blueshifting (up to approximately 150 THz) of the THz fields in the region of increasing free electron density.

The signal in Fig. 2.4 was low-pass filtered at 200 THz (as opposed to the 100 THz filter applied in Fig. 2.2) to include the peak frequency of the on-axis, blue-shifted THz field (around 150 THz at $z = -2$ cm). While the peak frequency is larger on axis, most of the THz field energy is distributed off axis where the average frequency is lower (≈ 50 THz).

The front velocity is extracted from Fig. 2.4 by measuring the slope of the null lines of $\partial_\tau J$. We find that the front velocity is approximately $v_f = 0.999\,95c$. For comparison, the 800 nm group velocity is $v_{g,800\text{ nm}} = 0.999\,72c$. With this front velocity and the refractive index model discussed above, the Cherenkov model predicts an off-axis angle of $\phi \approx 1.2°$ [according to Eq. (2.11)], which is similar to 0.9°, the value seen in Fig. 2.2.

Finally, we note the space-time dependence of the time derivative of the current density is not of the form required to produce Eq. (2.12) (except when $k_d \approx 0$). There is variation of the waveform with z, in addition to translation at v_f. The amplitude of $\partial_\tau J$ grows and the frequency increases over a distance of 3 cm. However the behavior is not a periodic oscillation with a clearly identifiable wave number k_d.

2.3.2 Angular Dependence of THz on Refractive Index

To test the model giving rise to Eq. (2.11) we attempt to vary v_{THz}. Competing propagation effects in the simulation make control of the current front velocity challenging. The THz phase velocity, on the other hand, can be directly manipulated by modifying the refractive index at THz frequencies. The resulting change in the simulated THz emission angle can then be compared to predictions of the Cherenkov model. Specifically, we use the following modified refractive index model;

$$\delta n(\omega) = \begin{cases} \delta n_0, & \omega/2\pi < 190\,\mathrm{THz} \\ \delta n_{\mathrm{PK}}(\omega), & \text{otherwise,} \end{cases} \tag{2.13}$$

where $n(\omega) = 1 + \delta n(\omega)$ and $\delta_{\mathrm{PK}}(\omega)$ is defined in Eq. (2.3). While the modified refractive index has no frequency dependence below 190 THz, the relative change in the actual refractive index of N_2 is only 0.2 % between 0 and 190 THz [36]. In all cases, the group velocity at low frequencies in N_2 is not significantly different than the phase velocity. Experimentally, the dispersion at low frequencies could be modified by the selection and relative percentage of gas species in the medium.

Figure 2.6 shows the extracted THz electric field for $\delta n_0 = 0$, 2.78×10^{-4}, and 1.1×10^{-3}. The propagation angle of the THz radiation can be seen to increase with increasing δn_0, as anticipated by Eq. (2.11). The variations of δn_0 leave the pump pulses and current front velocity largely unchanged. The pump pulses drive the current source and indirectly control the front velocity. Changes to the pump-

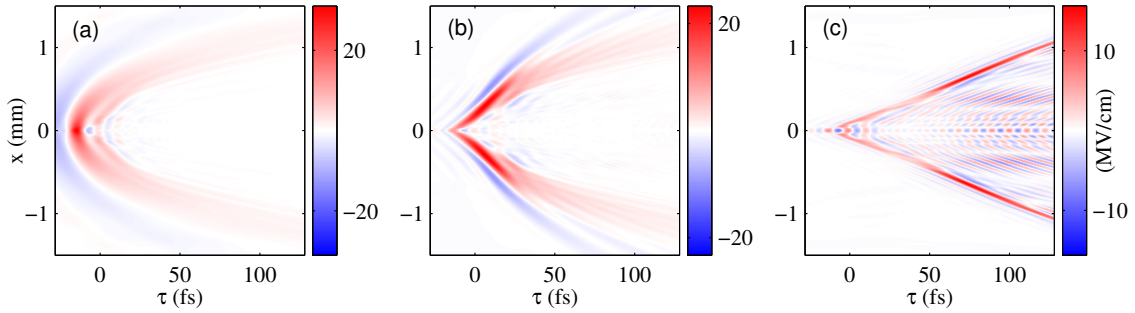

Figure 2.6: Shows the electric field at 1 cm before vacuum focus from 0 to 100 THz for three different THz dispersion models; $\delta n_0 = 0$, 2.78×10^{-4}, and 1.1×10^{-3} for (a), (b), and (c) respectively. Most of the THz have been generated at this point.

pulses' propagation, due to changes in the THz refractive index, should only occur via nonlinear interactions with the THz frequencies, e.g. non-degenerate four-wave mixing. These interactions tend to be smaller than the nonlinear processes involving the pump pulses alone.

The dependence of the THz propagation angle, ϕ, on δn_0 is shown in Fig. 2.7. For each δn_0, the THz angle is extracted from images such as those in Fig. 2.6 after most of the THz radiation has been generated, $z = -1$ cm. The simulation results are bounded by the Cherenkov model, Eq. (2.11), evaluated with v_f equal to the group velocity of 800 nm ($0.999\,72c$) and the extracted front velocity, $v_f = 0.999\,95$, from the simulations. This shows reasonable agreement between the predicted Cherenkov model and our simulations. The blue dotted curves in Fig. 2.7 show the predicted angle for the positive (lower curve) and negative (upper curve) solutions of Eq. (2.12). We substitute $k_d = \pi/L_\pi$ with $L_\pi = 3$ cm which is roughly the distance over which the THz current waveform varies. In this way Eq. (2.12) can be used to indicate the degree of uncertainty in the prediction of Eq. (2.11).

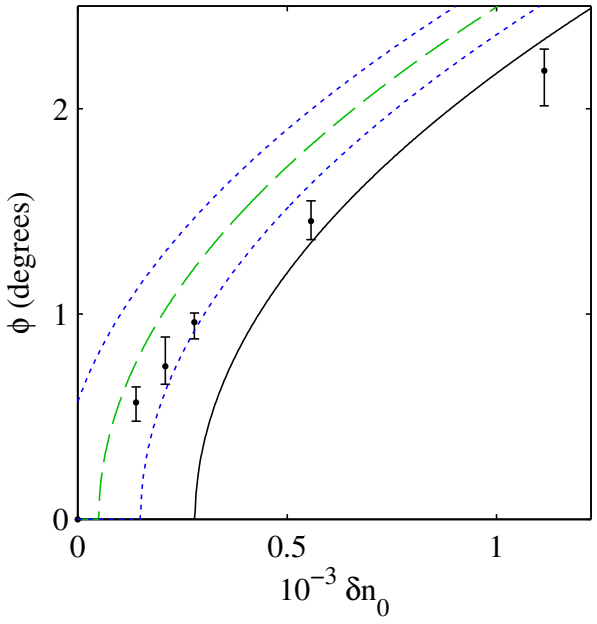

Figure 2.7: The dots with error bars are measured THz angle at $z = -1$ cm for separate simulations with a refractive index given by Eq. (2.13). The curves are Eq. (2.11) with fixed v_f and v_{THz} determined by the refractive index at $\omega = 0$. The solid black and dashed green curves are specifically for $v_f = 0.999\,72c$ and $v_f = 0.999\,95c$. The dotted blue curves are from Eq. (2.12) when the frequency is 50 THz, the dephasing length is 3 cm, and the front velocity is $0.999\,95c$.

2.3.3 Cherenkov Radiation from Four-Wave Mixing

In simulations, the free electron current is the dominant mechanism for generation of THz radiation [31]. When the current source, $\partial_\tau J$, and the effective loss current are removed from Eq. (2.2) using a high-pass filter, the third-order nonlinearities [the first term in Eq. (2.2)] still generate THz radiation as seen by the dashed curve in Fig. 2.5. But in this scenario, the conversion efficiency from pump-pulses' energy to THz is a factor of ≈ 40 times smaller than the photocurrent model. This is similar to results reported in [31]. Interestingly, the THz generated via four-wave mixing is also conical, suggesting that the optical Cherenkov mechanism is still at play. Figure 2.8 shows the THz field that is generated from four-wave interaction alone. The THz angle is the same as that of Fig. 2.2. This is expected since the bound nonlinear polarization current, which drives the THz, will follow the superluminal intensity fronts of the pump pulses.

2.3.4 Experimental Comparison

While the simulations seem to predict a THz propagation angle of $\approx 1^\circ$, You *et al.* observe THz radiation at angles of $\approx 4^\circ$ [16]. In the experiment, the focus was on frequencies below 10 THz as opposed to the broadband radiation below 100 THz that we have investigated. Blank *et al.* [45] observed a THz intensity spectrum that extends up to 100 THz with an off-axis angle of 3.2°. Their experiments are performed in air with similar parameters to ours: a pump-pulse energy of 0.42 mJ, fundamental wavelength of 775 nm, pump-pulse duration below 20 fs, and a focal

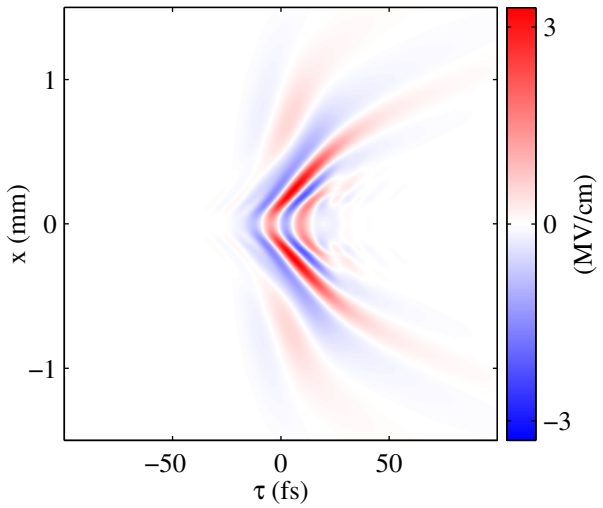

Figure 2.8: The electric field from 0 to 100 THz is shown in the transverse spatial dimension, x, versus a time window that is co-moving with the 800 nm pulse, τ. This THz electric field comparable to that of Fig. 2.2, except that this one was generated exclusively by a four-wave rectification process.

length of 20 cm. We find, if we further filter the THz signal, the average off-axis angle from the electric field power spectrum for frequencies between 5 and 10 THz to be $2.1° \pm 1.0°$. This is closer to the experimentally measured values. Differences still remain between the conditions in our simulations and the experiments. The simulated medium is N_2 as opposed to air. The index of refraction of air in the 10 THz range may have a frequency dependence not contained in our simulations. Also, the presence of oxygen, with a lower ionization potential than N_2, could lead to more free electrons and a different THz current source speed. Finally, the simulations are two dimensional. The superluminal front velocity is due to the focusing of the pump pulses. This speed can then be altered in going from two to three dimensions.

2.4 Directing THz Using Tilted-Intensity Fronts

The few cycle THz pulses that are created by the two-color mechanism can have a conical radiation patten. Experimentally, the THz pulses are observed at angles of 4° to 7° [16] and, in two-dimensional simulations, at angles of 1° to 2° [18]. By using a two-color pump pulse with fronts of constant intensity that are tilted with respect to the laser's phase fronts, the resulting THz is emitted directionally, instead of conically, and the THz angle can be controlled. This provides a mechanism for creating better collimated few cycle THz pulses.

A simple example of a tilted intensity front laser pulse is a Gaussian envelope with a transverse spatial chirp, or in other words, a transverse wavenumber k_x. The resulting single-color laser field is given by $E \propto \exp\left[-\tau^2/(2T^2)\right] \exp\left[-x^2/(2R^2)\right] \exp\left[ik_z z + ik_x x - i\omega t\right]$, where the time in the group velocity frame is $\tau = t - z/v_g$, the pulse duration is T, and the spot size is R. Lines of constant laser intensity would form concentric ellipses with the axes parallel and perpendicular to the x and τ axes, but the phase fronts of the electric field would be tilted by an angle $\theta_t = \tan^{-1}(k_x/k_z)$. While this is a tilted intensity front pulse, it is an inconvenient representation for laser propagation simulations because the laser pulse would propagate off of the z axis and out of the simulation domain. A more practical representation is when the Gaussian profile is rotated with respect to the z axis instead of the wavenumber. The electric field of a Gaussian laser pulse with tilted intensity fronts can be specified by using coordinates that have been rotated by the tilt angle θ_t; $E \propto \exp\left[-\bar{\tau}^2/(2T^2)\right] \exp\left[-\bar{x}^2/(2R^2) \exp\left[-i\omega\tau\right]\right]$, where the tilted

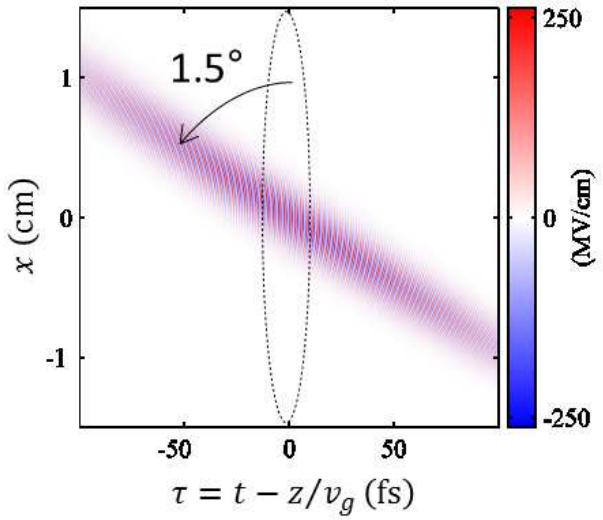

Figure 2.9: The laser electric field is shown in the transverse spatial dimension, x, versus a time window that is co-moving with the 800 nm pulse, τ. The intensity fronts of this pulse have been tilted by 1.5°.

time coordinate is $\bar{\tau} = \tau \cos\theta_t + (x/c)\sin\theta_t$, and the tilted transverse coordinate is $\bar{x} = -c\tau \sin\theta_t + x\cos\theta_t$. For example, a two-color laser pulse with a 1.5° tilt is shown in Fig. 2.9.

Tilted intensity front pulses can be created by reflecting a laser pulse off of a diffraction grating to impart the necessary transverse wavenumber [46]. For a two-color laser pulse, each color could be tilted independently and then recombined as was done in earlier two-color THz work [14].

For a two-color, tilted intensity front pulse, such as that in Fig. 2.9, the resulting THz pulse can be seen in Fig. 2.10. The laser and gas parameters are similar to those of Section 2.3 except for a $\theta_t = 1.5°$ tilt in the laser pulse. The resulting THz radiation in Fig. 2.10 is preferentially propagating in one direction. This is different than the Cherenkov emissions which occur in two directions as seen in Fig.

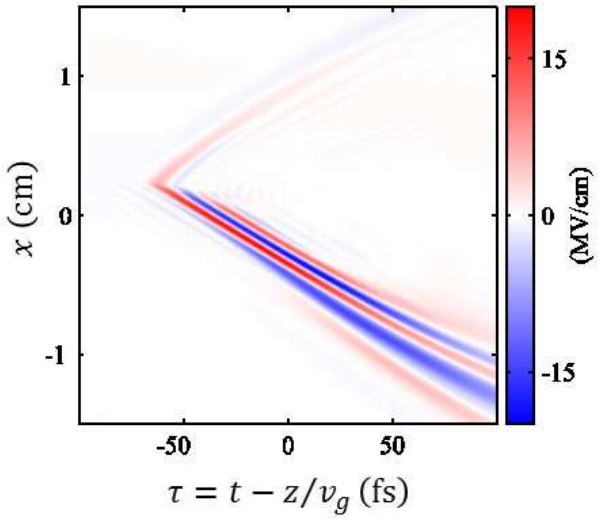

Figure 2.10: The electric field from 0 to 100 THz is shown in the transverse spatial dimension, x, versus a time window that is co-moving with the 800 nm pulse, τ.

2.2. Additionally, the THz emission angle can be controlled by changing the tilt angle, as in Fig. 2.11.

The theoretical model for the two-color Cherenkov mechanism can be expanded upon to capture the behavior of the THz emission from tilted intensity fronts. See Appendix 2.B.2 for details. For the Cherenkov emission, the THz current source was modeled as a spatially (transverse) localized source, but for two-color laser pulses with tilted intensity fronts a transverse profile is key.

2.5 Conclusion

We have developed a two-dimensional, unidirectional, electromagnetic propagation code to examine two-color THz generation in N_2. The model includes linear dispersion to all orders, the instantaneous and delayed-rotational nonlinear bound

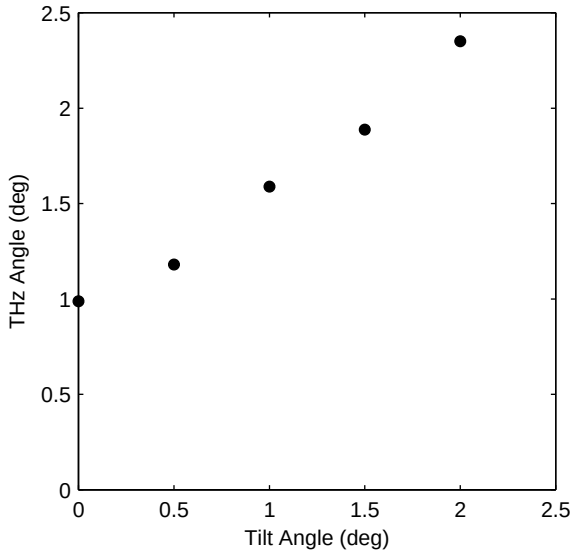

Figure 2.11: The angle of the THz pulse is shown as a function of the laser pulse tilt angle.

response, free electron generation via multiphoton and tunneling ionization, plasma response including collisional momentum damping, and ionization energy depletion. We have found that the off-axis, THz generation predicted by the simulations can be explained as an optical Cherenkov process. The angle of THz emission depends sensitively on the low frequency refractive index and current front velocity. Using our best estimate of the frequency dependent refractive index produces reasonable agreement with the experiment. Although the THz radiation is generated predominately by the photocurrent mechanism, the Cherenkov process also determines the emission angle of THz radiation generated by two-color, four-wave interaction in the nonlinear molecular polarizability. By using laser pulses with tilted intensity fronts, the THz radiation can be directed into one direction and the emission angle can be controlled.

2.A Hybrid Ionization Rate

MPI and TI are distinct limiting cases of a more general nonlinear photoionization theory such as that of Keldysh [47, 48] or later refinements by PPT and others [41, 49]. These limiting cases are roughly delineated by the Keldysh parameter $\gamma = \omega\sqrt{2m_e U_i}/(e\mathcal{E})$, where m_e and e are the electron mass and charge, while $\mathcal{E}$ is the electric field amplitude. For ease of calculation, the Keldysh parameter can be expressed as $\gamma = 6.4 \times 10^{12}\sqrt{U_i\,[\mathrm{eV}]}/(\lambda\,[\mathrm{nm}]\,\mathcal{E}\,[\mathrm{V/m}])$, where λ is the wavelength. For example, $\gamma \gg 1$ implies the multiphoton regime, while $\gamma \ll 1$ implies the tunneling regime. Typical parameters of the pump pulse during THz generation are $\lambda = 800$ nm and $\mathcal{E} \approx 4 \times 10^{10}$ V/m. The resulting Keldysh parameter is $\gamma \approx 0.8$ which is at the boundary between multiphoton and tunneling ionization.

As the pump pulses focus, the field strength will transition from the multiphoton to the tunneling regime. In the multiphoton regime, the TI rate underestimates free electron generation. Therefore, the decreased refractive index associated with the multiphoton generated free electrons can defocus the pump pulses and modify subsequent propagation more than expected from a TI rate. Unfortunately, the PPT ionization rate, which covers both regimes, is for a single color and dependent on the intensity, not on the instantaneous electric field. Therefore, it does not generate THz radiation according to the mechanism of interest.

The motivation for the hybrid ionization rate is to capture both the instantaneous nature of the tunneling ionization rate when in the tunneling regime, while not significantly underestimating free electron generation and defocusing effects when

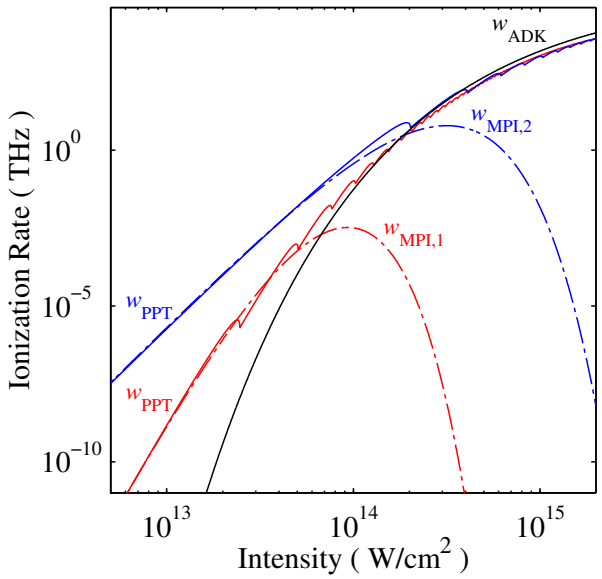

Figure 2.12: The solid red and blue curves represent PPT ionization rates for $\lambda = 800\,\text{nm},\ 400\,\text{nm}$ respectively. The solid black curve indicates a cycle-averaged tunneling rate which approaches the PPT rate at high intensities. The dashed-dotted red and blue curves show the MPI rates for $\lambda = 800\,\text{nm},\ 400\,\text{nm}$ respectively. Notice that a single color MPI rate plus the tunneling rate is a reasonable approximation of the associated PPT rate.

in the multiphoton regime.

Conventional MPI rates depend on the intensity to a large power [50]. This poses a problem when attempting to approximate the PPT ionization rate by interpolating from the multiphoton to the tunneling regime, e.g., by summing the MPI and TI rates. The problem arises because the MPI rate is orders of magnitude larger than the TI rate when evaluated in either the multiphoton or tunneling regimes. Therefore, the sum of the individual rates is always dominated by MPI. This is beneficial in the multiphoton limit but not in the tunneling limit where the tunneling rate should be a reasonable approximation. We adapt the MPI rate to drop exponentially with increasing intensity, as shown by the dashed-dotted red and blue curves of Fig. 2.12. The modified MPI rate is then summed with the tunneling

ionization rate to yield our single-color hybrid ionization rate. The cutoff intensity used in the exponential decay, I_{cutoff}, becomes a free parameter that is used to match $w_{\text{MPI,i}} + w_{\text{ADK}}$, after cycle averaging, to the PPT ionization rate for each color [41].

We then extend this hybrid ionization rate for two-color pulses. In the tunneling limit, the ionization rate should depend on the instantaneous field and therefore the Ammosov-Delone-Krainov (ADK) model should capture the two-color ionization dynamics [51, 52]. But in the multiphoton regime, the rate is strongly dependent on the frequency. In general, a nonlinear process like ionization is not additive in the individual rates. It is possible that mixed-photon ionization channels, like those involving N 800 nm photons and M 400 nm photons, would have important contributions to the total ionization rate. But summing the 800 nm and 400 nm MPI rates provides a better lower bound on the free electron generation in the multiphoton regime than neglecting either or both. Additionally, it provides a rate that can be fit to the accepted PPT rates in the limits of a laser pulse of either color. The absence of computationally efficient, quantum mechanical, atomic or molecular response models necessitates approximation. To this end, we treat the total MPI rate as the sum of the rates for the individual harmonics.

The full two-color hybrid ionization rate is given by

$$w[E] = w_{\text{MPI},1}(I_1) + w_{\text{MPI},2}(I_2) + w_{\text{ADK}}(E), \tag{2.14}$$

where I_1 and I_2 are the enveloped intensities of the fundamental- and second-harmonic pulses, respectively. The individual MPI rates are given by $w_{\text{MPI},i} =$

$\sigma_i I_i^{N_i} \exp\left(-I_i/I_{\text{cutoff},i}\right)$, where $\sigma_1 = 4.47 \times 10^{-140}$ $\text{cm}^{22}\,\text{W}^{-11}\,\text{s}^{-1}$, $N_1 = 11$, $I_{\text{cutoff},1} = 8.46 \times 10^{12}$ W/cm^2, $\sigma_2 = 2.46 \times 10^{-72}$ $\text{cm}^{12}\,\text{W}^{-6}\,\text{s}^{-1}$, $N_2 = 6$, and $I_{\text{cutoff},2} = 5.29 \times 10^{13}$ W/cm^2. The tunneling rate used is outlined in [51] with an ionization potential of $U_i = 15.576$ eV and effective Coulomb barrier $Z_{\text{eff}} = 0.9$ [52].

In the tunneling regime, Eq. (2.14) approximates the instantaneous ADK tunneling rate [51]. In the limit of a single color, either 800 or 400 nm, Eq. (2.14) after cycle averaging approaches the PPT rate for that color [41]. This implies that in the multiphoton limit and in the limit of a single color, Eq. (2.14) also matches the MPI rate.

As a result of enveloping, I_1 and I_2 do not depend on their respective carrier or carrier-envelope phases. This is consistent with traditional MPI models, which depend on the cycle-averaged field [50]. There has been recent theoretical work on the phase dependence of two-color MPI [53], but it does not lend itself to efficient numerical implementation in an electromagnetic propagation code. There has been work on computationally efficient ionization models [54] but work remains before implementation in a propagation code.

2.B Derivation of THz Spectrum

This appendix will derive the THz spectrum that results from the two-color Cherenkov process with and without tilted intensity fronts. Ideally, it would be possible to assert the initial two-color laser pulse and self consistently solve for the THz frequency currents and resulting fields, but this is not the case. The propagation

of the two-color pump pulse will be ignored and THz frequency source current it drives will be asserted. The assumed form of the THz frequency source current is based on observations of numerical simulations. The spectrum of the THz frequency electric fields, those that are driven by the source current, will be derived for three spatial dimensions. The limit to two spatial dimensions will be taken at the end.

The unidirectional pulse propagation equation with the free electron current as the driving term is

$$[\partial_z - ik_z(k_x, k_y, \omega)]\, \widehat{E}(k_x, k_y, z, \omega) = -\frac{\mu_0}{2ik_z(k_x, k_y, \omega)} \widehat{\partial_t J}(k_x, k_y, z, \omega), \qquad (2.15)$$

where the z component of the wavenumber is specified by the x and y components and the frequency using $k_z(k_x, k_y, \omega) = [\omega^2 n(\omega)^2/c^2 - k_x^2 - k_y^2]^{1/2}$. The linear refractive index of the gas is frequency dependent and given by $n(\omega)$. The spectrum of the electric field at each z position is specified by $\widehat{E}(k_x, k_y, z, \omega)$ using the transformation $\widehat{E}(k_x, k_y, z, \omega) = \int_{-\infty}^{\infty} E(x, y, z, t) \exp[-i(k_x x + k_y y - \omega t)]\, dx\, dy\, dt$. The spectrum of the current source $\widehat{\partial_t J}(k_x, k_y, \omega, t)$ is similarly defined. Issues with the zero frequency limit of Eq. (2.15) can be corrected by including collisional damping to the current model, as was done in the simulations.

In simulations, the current at THz frequencies is driven dominantly by the two-color pump pulse and the two-color pump is largely unaffected by the THz. Therefore, a fixed pump pulse will be assumed and for the UPPE, Eq. (2.15), it is only nessecary to consider how the THz electric fields develop with z. The resulting UPPE equation with functional dependences dropped would be $[\partial_z - ik_z]\, \widehat{E}_{\mathrm{THz}} =$

$-[\mu_0/(2ik_z)]\widehat{\partial_t J}_{\text{pump}}$.

The THz spectrum of the electric field can be solved for in general as an integral of the two-color pump pulse's source current over the propagation distance

$$\widehat{E}_{\text{THz}}(k_x, k_y, z, \omega) = -\frac{\mu_0}{2ik_z(k_x, k_y, \omega)} \int_0^z dz' \widehat{\partial_t J}_{\text{pump}}(k_x, k_y, z', \omega) e^{ik_z(k_x, k_y, \omega)(z-z')}, \tag{2.16}$$

with the initial condition that $\widehat{E}_{\text{THz}}(k_x, k_y, 0, \omega) = 0$.

2.B.1 Spectrum of Cherenkov Emission

An idealized current source must be constructed to approximate the key features of what is observed in simulations. For simplicity, the current source $\widehat{\partial_t J}_{\text{pump}}$ is treated as localized on the optical axis by using delta functions in the transverse dimensions. Additionally, the front of the current source is treated as a step function that moves at a speed $v_f \approx c$. A resulting free electron current is

$$J_{\text{pump}}(x, y, z, t) = I_0 \cos(k_d z + \theta_0)\delta(x)\delta(y)\theta(t - z/v_f), \tag{2.17}$$

where I_0 is the current with units of amperes. The $\cos(k_d z + \theta_0)$ is included to model the effect of the sign of the current oscillating over a distance of $2L_\pi = 2\pi/k_d$, where L_π is the dephasing distance. The sign of the current at $z = 0$ is set by the initial phase θ_0. The oscillating of the currents sign could be caused by phase velocity mismatch between the two colors in the pump pulse and is the mechanism for conical THz radiation in Ref. [16]. The oscillating currents can be neglected by

taking $k_d \to 0$ and $\theta_0 = 0$.

Before using Eq. (2.16) a time derivative must be taken of Eq. (2.17), yielding $\partial_t J_{\text{pump}}(x, y, z, t) = I_0 \cos(k_d z + \theta_0)\delta(x)\delta(y)\delta(t - z/v_f)$. This highlights the need for an assumed source current model with a differential time-dependence.

The final form of the electric field's THz spectrum is given by using Eqs. (2.16) and (2.17) to get

$$\left|\widehat{E}_{\text{THz}}(k_x, k_x, z, \omega)\right|^2 = \frac{\mu_0^2 I_0^2}{16 k_z^2(k_x, k_y, \omega)} \left|f(k_x, k_y, z, \omega)\right|^2 z^2, \tag{2.18}$$

where $k_\pm = \omega/v_f \pm k_d - k_z(k_x, k_y, \omega)$ and,

$$\begin{aligned} |f(k_x, k_y, z, \omega)|^2 = \big[&\text{sinc}^2(k_+ z/2) + \text{sinc}^2(k_- z/2) \\ &+ 2\cos(k_d z + 2\theta_0)\text{sinc}(k_+ z/2)\text{sinc}(k_- z/2)\big]. \end{aligned} \tag{2.19}$$

The angle of the THz radiation off of the z axis, ϕ, is given by $k_z = k\cos\phi$, where $k = \omega/v_{\text{THz}}$, and v_{THz} is the THz phase velocity. The sinc functions will be largest when $k_\pm = 0$, which provides a way to estimate the angle of the THz radiation. For example, there are two possible angles $\phi_\pm$ when $k_\pm = 0$ and they are given by $\cos\phi_\pm = v_{\text{THz}}/v_f \pm [\lambda/(2L_\pi)](v_{\text{THz}}/c)$. If the sign of the THz current doesn't slowly oscillate with propagation distance, i.e. $k_d = 0$, then $k_+ = k_-$ and then the electric field spectrum will go like $|f(k_x, k_y, z, \omega)|^2 = 4\text{sinc}^2\left[(\omega/v_f - (\omega/v_{\text{THz}})\cos\phi)\, z/2\right]$.

To achieve more realistic source currents, other spatio-temporal profiles can be created. Tractable solutions have been found for cylindrical or Gaussian transverse spatial profiles and for smooth ramps, such as the error function, for the time

dependence of the current. Additionally, the current source can be given a central frequency at which it drives THz. Unfortunately, using the more complicated current model does not yield greatly improved predictive ability because, with the more realistic appearing source currents, there are an increasing number of free parameters.

The result for two-dimensional planar geometry is given below. In this situation, the previous results can be used in the limit that $k_y \to 0$ and the current I_0 becomes the current per unit length

$$\left|\widehat{E}^{\mathrm{2D}}_{\mathrm{THz}}(k_x, z, \omega)\right|^2 = \frac{\mu_0^2 I_0^2}{16 k_z^2} \left|f(k_x, 0, z, \omega)\right|^2 z^2, \tag{2.20}$$

where $k_z = \sqrt{\omega^2 n^2/c^2 - k_x^2}$.

2.B.2 Spectrum from Tilted Intensity Fronts

The derivation for the two-color Cherenkov spectrum can be extended to capture the effect of a pump pulse with tilted intensity fronts. The time rate of change of the current, i.e. , the current source $\partial_\tau J_{\mathrm{pump}}$, will be assumed to have a transverse length scale σ_x and temporal duration σ_t. These scales are smaller than those of the two-color laser pulse, but are still the same order of magnitude. The main assumption is that the current source has the same tilted intensity front profile as the electric field. The current source is Gaussian along the coordinates $\bar{x}$ and $\bar{t}$. These coordinates are rotated by θ_t with respect to x and τ. A positive rotation of $\theta_t > 0$ corresponds to a pulse with a positive average $\langle k_x \rangle > 0$ such that $\langle k_x \rangle \,/\, \langle k_z \rangle = \tan\theta_t$.

In the rotated coordinates $(\bar{x}, \bar{y}, \bar{t})$ the laser field and the resulting current source have the form of a Gaussian

$$|\partial_t J_{\text{pump}}(x, y, z, t)| \propto e^{-\bar{x}^2/(2\sigma_x)^2} e^{-\bar{y}^2/(2\sigma_x)^2} e^{-\bar{\tau}^2/(2\sigma_t)^2}. \tag{2.21}$$

where $\tau = t - z/v_g$ is time in the frame moving with the group velocity. We expect that a rotation will relate $(\bar{x}, \bar{y}, \bar{\tau})$ and (x, y, τ).

$$\begin{aligned} \bar{x} &= x\cos\theta_t - \tau c \sin\theta_t \\ \bar{y} &= y \\ \bar{\tau} &= \frac{x}{c}\sin\theta_t + \tau\cos\theta_t \end{aligned} \tag{2.22}$$

The current source expressed in We choose the rate of change of the current to have a the same tilted front profile as the laser pulse except instead of moving at the group velocity the current source as allowed to move at the front velocity v_f, so $\tau = t - z/v_f$ and

$$\begin{aligned} \partial_t J_{\text{pump}} =& \frac{I_0}{8\sqrt{\pi}\sigma_t(\pi\sigma_x\sigma_y)} e^{-\left(x\cos\theta_t - (t-z/v_f)c\sin\theta_t\right)^2/(2\sigma_x)^2} e^{-y^2/(2\sigma_y)^2} \\ & \times e^{-\left((x/c)\sin\theta_t + (t-z/v_f)\cos\theta_t\right)^2/(2\sigma_t)^2}. \end{aligned} \tag{2.23}$$

The prefactor for the $\partial_t J_{\text{pump}}$ is such that $\pi\sigma_x\sigma_y$ is the cross-sectional area of the current source, σ_t is the temporal duration, and I_0 is the total current. This source current will limit to that of the Cherenkov model when $\sigma_x, \sigma_y, \sigma_t \to 0$. In Eq. (2.16),

the THz field depends on the source current in the spectral domain

$$\begin{aligned}\widehat{\partial_t J}_{\text{pump}} =& \frac{I_0}{8\sqrt{\pi}\sigma_t(\pi\sigma_x\sigma_y)} \int dxdydte^{-ik_x x - ik_y y + i\omega t} \\ & \times e^{-\left(x\cos\theta_t - (t - z/v_f)c\sin\theta_t\right)^2/(2\sigma_x)^2} e^{-y^2/(2\sigma_y)^2} \\ & \times e^{-\left((x/c)\sin\theta_t + (t-z/v_f)\cos\theta_t\right)^2/(2\sigma_t)^2}.\end{aligned} \tag{2.24}$$

The transform becomes a three dimensional Gaussian if a change of variables is made from (x, y, t) to $(\bar{x}, \bar{y}, \bar{\tau})$

$$\begin{aligned}\widehat{\partial_t J}_{\text{pump}} =& \frac{I_0 e^{i\omega z/v_f}}{8\sqrt{\pi}\sigma_t(\pi\sigma_x\sigma_y)} \int d\bar{x}d\bar{y}d\bar{\tau} e^{-\bar{x}^2/(2\sigma_x)^2} e^{-\bar{y}^2/(2\sigma_y)^2} e^{-\bar{\tau}^2/(2\sigma_t)^2} \\ & \times e^{-ik_x(\bar{x}\cos\theta_t + \bar{\tau}c\sin\theta_t) - ik_y\bar{y} + i\omega(-\frac{\bar{x}}{c}\sin\theta_t + \bar{\tau}\cos\theta_t)}.\end{aligned} \tag{2.25}$$

The wavenumber components and frequency can be redefined so as to simplify Fourier transforms. This will correspond to a rotation in (k_x, k_y, ω)-space

$$\bar{k}_x = k_x\cos\theta_t + \frac{\omega}{c}\sin\theta_t, \tag{2.26}$$

$$\bar{k}_y = k_y, \tag{2.27}$$

$$\bar{\omega} = -k_x c\sin\theta_t + \omega\cos\theta_t. \tag{2.28}$$

The resulting spectrum of the source current in the rotated spectral coordinates is

$$\widehat{\partial_t J}_{\text{pump}} = I_0 e^{i\omega z/v_f} e^{-\bar{k}_x^2\sigma_x^2} e^{-\bar{k}_y^2\sigma_y^2} e^{-\bar{\omega}^2\sigma_t^2}. \tag{2.29}$$

After using Eq. (2.29) with Eq. (2.16) the electric field amplitude is

$$\widehat{A}_{\mathrm{THz}}(z) = -\frac{\mu_0 I_0}{2ik_z} e^{-\bar{k}_x^2\sigma_x^2} e^{-\bar{k}_y^2\sigma_y^2} e^{-\bar{\omega}^2\sigma_t^2} e^{-i\frac{1}{2}(k_z-\frac{\omega}{v_f})z} \mathrm{sinc}\left[\left(k_z - \frac{\omega}{v_f}\right)\frac{z}{2}\right] z. \tag{2.30}$$

The magnitude of the THz spectrum in the (k_x, k_y, ω) domain is

$$\left|\widehat{A}_{\mathrm{THz}}(z)\right|^2 = \left(\frac{\mu_0 I_0}{2k_z}\right)^2 e^{-2g(k_x,k_y,\omega)} \mathrm{sinc}^2\left[\frac{1}{2}\left(k_z - \frac{\omega}{v_f}\right) z\right] z^2 \tag{2.31}$$

with

$$g(k_x, k_y, \omega) = (k_x \cos\theta_t + \frac{\omega}{c}\sin\theta_t)^2\sigma_x^2 + k_y^2\sigma_y^2 + (-k_x \sin\theta_t + \frac{\omega}{c}\cos\theta_t)^2 c^2\sigma_t^2. \tag{2.32}$$

The function $g(k_x, k_y, \omega)$ is nonnegative and captures the part of the THz spectrum that is due to the finite bandwidth of the source current. The THz spectrum is largest where g is smallest. The minima of g can be found by separately minimizing in k_x and ω. This sets the axes of an ellipse

$$\text{axis (a):} \qquad +k_x^{(\mathrm{a})}\cos\theta_t + \frac{\omega}{c}\sin\theta_t = 0, \tag{2.33}$$

$$\text{axis (b):} \qquad -k_x^{(\mathrm{b})}\sin\theta_t + \frac{\omega}{c}\cos\theta_t = 0. \tag{2.34}$$

where the transverse wavenumber for principle axis (a) and (b) are given by $k_x^{(\mathrm{a})} = -(\omega/c)\tan\theta_t$ and $k_x^{(\mathrm{b})} = (\omega/c)\cot\theta_t$ respectively. Typically in ultrashort laser pulses the longitudinal (or temporal) dimension of the laser pulse is much smaller than the transverse dimension, i.e. , $c\sigma_t \ll \sigma_x$. As a result, σ_x is the dominant contribution

to $g(k_x, k_y, \omega)$ and axis (a) is the major axis of $g(k_x, k_y, \omega)$. For small tilt angles and in the absence of a Cherenkov effect, this is suggestive of the THz spectrum being biased to propagate off-axis at θ_t because $k_x/(\omega/c) \approx \tan\theta_t \approx \theta_t$.

Chapter 3: Remote Atmospheric Magnetometry

3.1 Introduction

Optical magnetometry is a highly sensitive method for measuring small variations in magnetic fields [55–57]. The development of a remote optical magnetometry system would have important applications for the detection of underwater and underground objects that perturb the local ambient magnetic field. In our remote atmospheric optical magnetometry model, a high-intensity pump laser pulse is employed to drive wakefields which have a rotated polarization due to the earth's magnetic field. This can, in principle, provide a means to measure variations in the earth's magnetic field. For a number of magnetic anomaly detection (MAD) applications, $10\,\mu$G magnetic field variations must be detected at standoff distances of approximately one kilometer from the sensor [22].

In this chapter, we consider molecular oxygen at atmospheric conditions as the paramagnetic species in a remote optical magnetometry configuration depicted in Fig. 3.1. The propagation of the high-intensity pump laser pulse to remote detection sites is considered. We show that high laser intensities (below $10^{12}\,\mathrm{W/cm^2}$ to avoid photoionization processes) can be propagated to remote locations due to the self focusing of the optical Ker effect. Using a linearly polarized, high-intensity laser

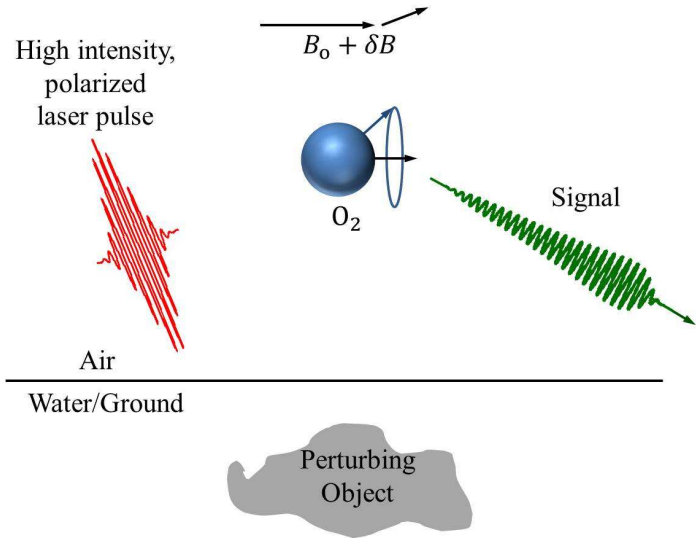

Figure 3.1: Remote optical magnetometry configuration. The earth's magnetic field is $B_0 \approx 0.5\,\mathrm{G}$ and $\delta B \approx 10\,\mu\mathrm{G}$ is the perturbation caused by the underwater/underground object.

pulse we consider the magnetization currents that are left ringing behind the pump pulse and the resulting co-propagating electromagnetic field. This field is referred to as the wakefield and it undergoes polarization rotation due to the Zeeman splitting of oxygen's ground state. The magnetic field variation is detected by measuring the wakefield's polarization.

Molecular oxygen's paramagnetic response is due to two unpaired valance electrons. The ground state of oxygen $X^3\Sigma_g^-$, commonly referred to as "triplet oxygen," has total angular momentum $J = 1$, total spin $S = 1$, and three degenerate sublevels. The excited upper state being considered is denoted by $b^1\Sigma_g^+$. It has $J = 0$ and is a spin singlet state $S = 0$ with only one sublevel. The upper state can undergo three radiative transitions, $b^1\Sigma_g^+ \rightarrow X^3\Sigma_g^-(m = \pm 1)$, $b^1\Sigma_g^+ \rightarrow X^3\Sigma_g^-(m = 0)$, but the latter is insignificant because it is an electric quadruple transition. There is an intermediate state, referred to as $a^1\Delta_g$, into which the excited O_2 molecule can

decay and is discussed in Appendix 3.A. The O_2 transition line being considered is the $b^1\Sigma_g^+ - X^3\Sigma_g^-$ transition band of oxygen near 762 nm. In the low intensity, long laser pulse, regime, this transition has been investigated theoretically [23, 24] and experimentally [25] and is a prominent feature of air glow. A high intensity, polarized titanium-doped sapphire laser is considered for the pump laser. These lasers have an extremely large tuning range from 660 nm to 1180 nm, and can have linewidths that are transform limited.

A major challenge for this, as well as any remote atmospheric optical magnetometry concept, is collisional dephasing (elastic collisions) of the transitions. The elastic molecular collision frequency, at standard temperature and pressure (STP), is $\gamma_c = N_{\text{air}}\sigma v_{th} = 3.5 \times 10^9\,\text{s}^{-1}$, where σ is the molecular cross section and v_{th} is the thermal velocity [25]. On the other hand, the Larmor frequency in the earth's magnetic field is $\Omega_0 = qB_0/(2mc) \approx 4.5 \times 10^6\,\text{rad/s}$ ($\hbar\Omega_0 = 3 \times 10^{-9}\,\text{eV}$), where m and q are the electron mass and charge and c is the speed of light. Since the dephasing frequency is far greater than the Larmor frequency, the parameters are somewhat restrictive for remote atmospheric magnetometry. However, rotational magnetometry experiments based on molecular oxygen at STP and magnetic fields of $\sim 10\,\text{G}$ have shown measurable linear Faraday rotational effects [25].

Previous theoretical work [24] revealed major issues with atmospheric magnetic field measurements using oxygen, these include: (1) extremely low photon absorption cross sections, (2) a broad magnetic resonance linewidth due to collisions, and (3) quenching of excited-state fluorescence. These issues largely stem from oxygen's small magnetic dipole moment and large collision rate. In our work,

however, the wakefield's polarization rotation is the magnetic signature and the laser pulse intensities are approximately six orders of magnitude larger.

3.2 Focusing & Compression of Intense Laser Pulses

The magnetometry concept considered here relies on propagation of intense laser beams in the atmosphere. This propagation is strongly affected by various interrelated linear and nonlinear processes [43]. These include diffraction, Kerr self-focusing, group velocity dispersion, spectral broadening, and self-phase modulation. In general, a laser pulse propagating in air can be longitudinally and transversely focused simultaneously at remote distances ($\sim$ km) to reach high intensities ($\sim 10^{12}\,\mathrm{W/cm^2}$), as indicated in Fig. 3.2. Due to group velocity dispersion, pulse compression can be achieved by introducing a frequency chirp on the pulse; however, for the parameters under consideration, pulse compression is not significant. Nonlinear transverse focusing is caused by the optical Kerr effect.

Here, we present the model describing longitudinal and transverse compression of a chirped laser pulses in air [43]. The laser electric field is given by $\mathbf{E}(r,\eta,\tau) = (1/2)\widehat{E}(r,\eta,\tau)e^{-i\omega\tau}\widehat{\mathbf{e}}_x + \text{c.c.}$, where $\widehat{E}$ is the complex amplitude, ω is the frequency, r is the radial coordinate, $\tau = t - z/c$ and $\eta = z$ are the transformed coordinates, and the propagation distance z and time t are in the laboratory frame. Substituting this field representation into the wave equation results in an extension of the paraxial

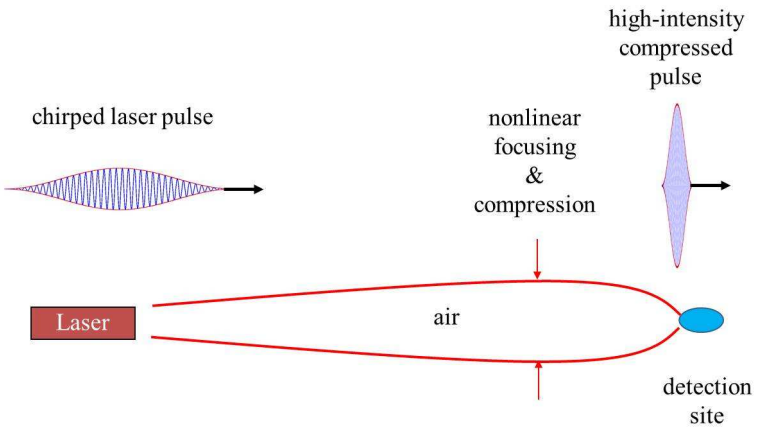

Figure 3.2: Simultaneous transverse focusing and longitudinal compression of a chirped ultrashort laser pulse in air due to nonlinear self-focusing and group velocity dispersion. For the 100 ps pulses that are optimal for magnetometry, longitudinal compression is negligible, but transverse self-focusing can compensate.

wave equation for $\widehat{E}(r,\eta,\tau)$ [43],

$$\left[\nabla_\perp^2 + 2ik\frac{\partial}{\partial\eta} - c^2k\beta_2\frac{\partial^2}{\partial c^2\tau^2} + \frac{\omega^2 n_K}{4\pi c}\left|\widehat{E}(r,\eta,\tau)\right|^2\right]\widehat{E}(r,\eta,\tau) = 0, \qquad (3.1)$$

where the wavenumber is $k = \omega/c$. For air at STP and $\lambda = 2\pi/k \approx 762\,\text{nm}$, the group velocity dispersion is $\beta_2 = 2.2\times10^{-31}\,\text{s}^2/\text{cm}$, the Kerr nonlinear index is $n_K = 3\times10^{-19}\,\text{cm}^2/\text{W}$, and $1 + n_K I$ is the refractive index of air.

Equation (3.1) can be solved by assuming the pulse is described by a form that depends on certain spatially dependent parameters. With this assumption, a set of simplified coupled equations can be derived for the evolution of the spot size, pulse duration, amplitude, and phase of the laser field. Taking the laser pulse to have a Gaussian shape in both the transverse and longitudinal directions, the complex

amplitude can be written as

$$\widehat{E}(r,\eta,\tau) = \widehat{E}_0(\eta) e^{i\theta(\eta)} e^{-(1+i\alpha(\eta))r^2/R^2(\eta)} e^{-(1+i\beta(\eta))\tau^2/T^2(\eta)}, \tag{3.2}$$

where $\widehat{E}_0(\eta)$ is the field amplitude, $\theta(\eta)$ is the phase, $R(\eta)$ is the spot size, $\alpha(\eta)$ is related to the curvature of the wavefront, $T(\eta)$ is the laser pulse duration, and $\beta(\eta)$ is the chirp parameter. The $\widehat{E}_0$, θ, T, R, α, β are real functions of the propagation distance η. The instantaneous frequency spread along the pulse, i.e., chirp, is $\delta\omega(\eta,\tau) = 2\beta(\eta)\tau/T^2(\eta)$, where $\beta(\eta) = T(\eta)/\left(2\beta_2\right)\partial T(\eta)/\partial\eta$. A negative (positive) frequency chirp, $\beta(\eta) < 0$ ($\beta(\eta) > 0$), results in decreasing (increasing) frequencies towards the back of the pulse.

Substituting Eq. (3.2) into Eq. (3.1) and equating like powers of r and τ, the following coupled equations for R and T are obtained,

$$\frac{\partial^2 R}{\partial\eta^2} = \frac{4}{k^2R^3}\left(1 - \frac{\mathcal{E}_0}{P_{\rm NL}}\frac{1}{T}\right), \tag{3.3a}$$

$$\frac{\partial^2 T}{\partial\eta^2} = \frac{4\beta_2}{k}\frac{\mathcal{E}_0}{P_{\rm NL}}\frac{1}{R^2T^2} + \frac{4\beta_2^2}{T^3}, \tag{3.3b}$$

where $\mathcal{E}_0 = P(0)T(0)$ is proportional to the laser pulse energy and is independent of η, $P(\eta) = \pi R^2(\eta)I(\eta)/2$ is the laser power, $I(\eta) = c\widehat{E}_0^2(\eta)/(8\pi) = I(0)R^2(0)T(0)/(R^2(\eta)T(\eta))$ is the peak intensity, and $P_{\rm NL} = \lambda^2/(2\pi n_K)$ is the self-focusing or critical power. In Eq. (3.3) the initial conditions are given by $\alpha(0) = -(kR(0)/2)\partial R(0)/\partial\eta$ and $\beta(0) = T(0)/(2\beta_2)\partial T(0)/\partial\eta = 0$. The first term on the right hand side of Eq. (3.3a) describes vacuum diffraction while the second term describes nonlinear self-

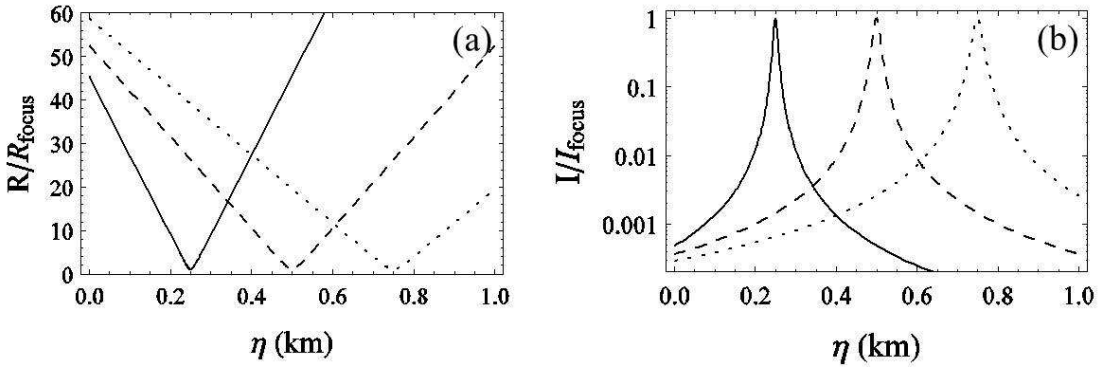

Figure 3.3: Evolution of (a) laser spot size and (b) normalized peak laser intensity as functions of propagation distance for different initial laser energies and spot sizes. The laser energy and initial spot size for the solid, dashed, and dotted lines are $\mathcal{E}_0 = 100$, 150, and 190 mJ and $R(0) = 4.7$, 6.7, and 8.2 cm, respectively. By tuning laser parameters, the remote detection region can be moved.

focusing, i.e., due to n_K. Nonlinear self-focusing dominates diffraction resulting in filamentation when $P > P_{\rm NL} \approx 3\,{\rm GW}$ [43, 50].

In the limit that the pulse length does not change appreciably, the laser spot size is given by $R(\eta) = R(0)[1 - 2\alpha(0)\eta/Z_{R0} + (1 - P/P_{\rm NL} + \alpha^2(0))\eta^2/Z_{R0}^2]^{1/2}$, where $Z_{R0} = kR^2(0)/2$ is the Rayleigh length. The spot size reaches a focus in a distance $\eta/Z_{R0} = \alpha(0)/\left(1 - P/P_{\rm NL} + \alpha^2(0)\right)$ as long as $P < \left(1 + \alpha^2(0)\right) P_{\rm NL}$.

Figures 3.3(a) and 3.3(b) show the evolution of the laser spot size and the intensity as a function of propagation distance for $\lambda = 762\,{\rm nm}$. At focus, the laser intensity $I_{\rm focus} = 6 \times 10^{10}\,{\rm W/cm}^2$ and spot size $R_{\rm focus} = 1.3\,{\rm mm}$ are held constant by choosing appropriate initial conditions: wavefront curvature $\alpha(0) = 37$, pulse duration $T(0) = 100\,{\rm ps}$, and chirp $\beta(0) = 0$. By changing the laser energy and the initial spot size, the nonlinear self-focusing effect changes the focal point from 0.25 km to 0.75 km (see Fig. 3.3). Nonlinear laser pulse propagation allows for moving of the detection site location.

To achieve high focal intensities at ranges from 0.25 km to 0.5 km without relying on atmospheric nonlinearities, i.e., Kerr index, would require focusing optics with diameters from 22 cm to 66 cm.

3.3 Optical Magnetometry Model

The four levels of O_2 being considered in the magnetometry model are shown in Fig. 3.4. The ground state is split by the Zeeman effect into three levels $|1\rangle$, $|2\rangle$, and $|3\rangle$ and the excited state is denoted by $|4\rangle$. The transition frequency with no Zeeman splitting corresponds to $\hbar\omega_A = 1.63\,\text{eV}$ (762 nm). The magnetic quantum number m associated with the various levels is indicated in Fig. 3.4. The excited state, level $|4\rangle$, can be populated by left hand polarized (LHP) light from level $|3\rangle$ or by right hand polarized (RHP) light from level $|1\rangle$. Here, the quantization axis and the direction of the static magnetic field are taken to be along the direction of laser propagation, the z-axis. Circularly polarized radiation carries angular momentum $\pm\hbar$, which is directed along the propagation direction. The selection rule for allowed transitions is $\Delta m = \pm 1$ which will conserve angular momentum [58]. It should be noted that this transition is strictly magnetic dipole and spin forbidden, but spin-orbit coupling between the $b^1\Sigma_g^+$ and $X^3\Sigma_g^-(m = 0)$ states leads to a transition with a magnetic dipole-like nature and a larger than expected dipole moment [23, 24, 59].

A high-intensity pump pulse generates a magnetization current density $\mathbf{J}_M = c\nabla \times \mathbf{M}$, where $\mathbf{M}$ is the magnetization field. The current density in turn generates a response electric field and can also modify the pump pulse. The re-

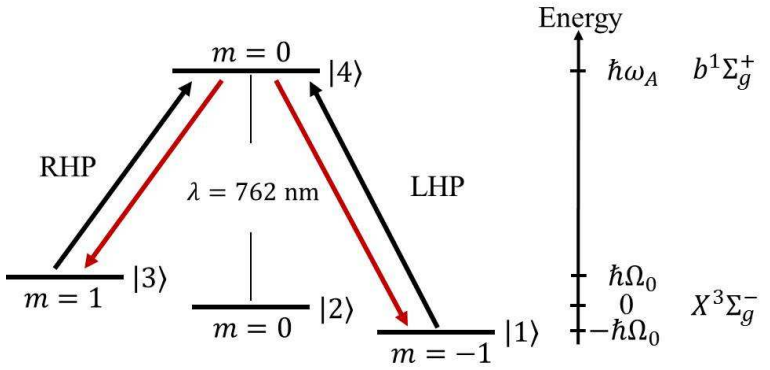

Figure 3.4: Energy levels associated with the ground and excited state of O_2. The transition frequency corresponds to $\hbar\omega_A = 1.63\,\text{eV}$ (762 nm). The Zeeman splitting of the ground state is caused by the ambient magnetic field.

sponse electric field $\mathbf{E}$ is given by $\left(\nabla^2 - (1/c^2)\,\partial^2/\partial t^2\right)\mathbf{E} = (4\pi/c^2)\,\partial\mathbf{J}_M/\partial t = (4\pi/c)\,\partial\left(\nabla\times\mathbf{M}\right)/\partial t$ (Gaussian units). The magnetization is represented by a sum of LHP and RHP components $\mathbf{M}(z,t) = M_L(z,t)\widehat{\mathbf{e}}_L + M_R(z,t)\widehat{\mathbf{e}}_R + \text{c.c.}$, where $M_L(z,t) = N\mu_m\rho_{43}(z,t)$, $M_R(z,t) = N\mu_m\rho_{41}(z,t)$, N is the density of the oxygen molecules, μ_m is the effective magnetic dipole moment associated with the transitions, ρ_{43} and ρ_{41} are the off-diagonal coherence of the allowed density matrix elements (see Fig. 3.4) and $\widehat{\mathbf{e}}_{L,R} = \left(\widehat{\mathbf{e}}_x \pm i\widehat{\mathbf{e}}_y\right)/2$ are vectors denoting the polarization direction. The magnetization current density can be written as $\mathbf{J}_M = -ic\partial M_L(z,t)/\partial z\widehat{\mathbf{e}}_L + ic\partial M_R(z,t)/\partial z\widehat{\mathbf{e}}_R + \text{c.c.}$ In terms of the x and y components, $\mathbf{J}_M = -i(c/2)\partial\left(M_L - M_R\right)/\partial z\widehat{\mathbf{e}}_x + (c/2)\partial\left(M_L + M_R\right)/\partial z\widehat{\mathbf{e}}_y + \text{c.c.}$

The density matrix equation is given by $\partial\rho_{nm}/\partial t = -i\omega_{nm}\rho_{nm} + i\sum_l(\Omega_{nl}\rho_{lm} - \Omega_{lm}\rho_{nl}) + \text{relaxation terms}$, where $\omega_{nm} = \omega_n - \omega_m$, Ω_{nm} denotes the interaction frequency, the phenomenological relaxation terms are due to elastic and inelastic collisions, and spontaneous transitions and the magnetic dipole interaction Hamiltonian

is $-\boldsymbol{\mu}_m \cdot \mathbf{B}$ (Appendix 3.B) [58, 60, 61]. The off-diagonal coherence elements of the density matrix for the relevant transitions, $|1\rangle \rightarrow |4\rangle$ and $|3\rangle \rightarrow |4\rangle$, are given by

$$\partial\rho_{41}/\partial t = -\gamma_c\rho_{41} - i\omega_{41}\rho_{41} + i\Omega_{41}\left(\rho_{11} - \rho_{44}\right) + i\Omega_{43}\rho_{31}, \tag{3.4a}$$

$$\partial\rho_{43}/\partial t = -\gamma_c\rho_{43} - i\omega_{43}\rho_{43} + i\Omega_{43}\left(\rho_{33} - \rho_{44}\right) + i\Omega_{41}\rho_{13}, \tag{3.4b}$$

where γ_c is the elastic collision frequency (not population transferring), the full set of density matrix equations are given in Appendix 3.B.

The pump laser field, which induces the magnetization field, is expressed as a sum of LHP and RHP fields $\mathbf{B}_{\text{pump}}(z,t) = B_L(z,t)\widehat{\mathbf{e}}_L + B_R(z,t)\widehat{\mathbf{e}}_R + \text{c.c.}$, where $B_{L,R}(z,t) = \widehat{B}_{L,R}(z,t)e^{i\psi(z,t)}$ and $\psi(z,t) = kz - \omega t$. The interaction frequencies associated with the allowed transitions are $\Omega_{43}(z,t) = \widehat{\Omega}_L(z,t)e^{i\psi(z,t)}$ and $\Omega_{41}(z,t) = \widehat{\Omega}_R(z,t)e^{i\psi(z,t)}$, where $\widehat{\Omega}_{L,R}(z,t) = \mu_m\widehat{B}_{L,R}(z,t)/\hbar$ is half the Rabi frequency associated with the LHP and RHP components of the pump. Note that the Rabi frequency is defined with respect to the peak field.

Although we are considering a magnetic dipole transition, it is convenient to express the Rabi frequency normalized to an electric dipole moment. The magnitude of the Rabi frequency can be written as $\widehat{\Omega}_{\text{Rabi}} = \mu_m\widehat{B}_{\text{peak}}/\hbar = (\mu_m/\mu_e)(\mu_e\widehat{E}_{\text{peak}}/\hbar) = (\mu_m/\mu_e)(\mu_e/\hbar)\left(8\pi I/c\right)^{1/2}$, where $I = c\widehat{E}^2_{\text{peak}}/(8\pi)$ is the pump laser intensity and $\widehat{E}_{\text{peak}}$ is the peak electric field. Taking the normalizing electric dipole moment to be $\mu_e = qr_B = 2.5\times10^{-18}\,\text{statC-cm}$, where r_B is the Bohr radius, the magnitude of the Rabi frequency is $\widehat{\Omega}_{\text{Rabi}}\,[\text{rad/s}] = 2.5\times10^8(\mu_m/\mu_e)\sqrt{I\,[\text{W/cm}^2]}$. As an example, for $I = 10^{11}\,\text{W/cm}^2$ and $\mu_m/\mu_e = 10^{-4}$, the Rabi frequency is $\widehat{\Omega}_{\text{Rabi}} = 8\times10^9\,\text{rad/s}$.

3.4 Faraday Rotation of Wakefields Driven by Intense Laser Pulses

The incident pump field is taken to be polarized in the x-direction $\mathbf{E} = \widehat{E}_0(z,t)e^{i(kz-\omega t)}(\widehat{\mathbf{e}}_L + \widehat{\mathbf{e}}_R) + \text{c.c.}$, where ω is the carrier laser frequency and the complex pulse amplitude $\widehat{E}_0(z,t)$ can be modulated. Employing the variables $\tau = t - z/c$ and $\eta = z$, $\mathbf{E} = \widehat{E}_0(\tau)e^{-i\omega\tau}e^{i\Delta k\eta}\,(\widehat{\mathbf{e}}_L + \widehat{\mathbf{e}}_R) + \text{c.c.}$, the corresponding magnetic field in the y-direction is $\mathbf{B} = -i\widehat{E}_0(\tau)e^{-i\omega\tau}e^{i\Delta k\eta}\,(\widehat{\mathbf{e}}_L - \widehat{\mathbf{e}}_R) + \text{c.c.}$, where $\Delta k = k - \omega/c$ is the wavenumber mismatch. The imaginary part of the wavenumber mismatch $\text{Im}[\Delta k] = \Gamma_D = (2\pi k N \mu_m^2 \rho_{11}\gamma_c/\hbar)((\omega-\omega_A)^2 + \gamma_c^2)^{-1}$ is obtained from the linear dispersion relation and accounts for absorption. The characteristic wavenumber mismatch for $\lambda = 762\,\text{nm}$ at atmospheric molecular oxygen density $N = 5.7\times10^{18}\,\text{cm}^{-3}$ and an equilibrium population of $\rho_{11} = 1/3$ is $\Gamma_D = 1.7\times10^{-2}\,\text{cm}^{-1}$ $(1/\Gamma_D \approx 60\,\text{cm})$. To circumvent this short absorption length, the laser frequency can be moved off-resonance. For example, if we detune the laser by $30\gamma_c$, which corresponds to a wavelength shift of $0.03\,\text{nm}$, then the absorption length is $1/\Gamma_D \approx 500\,\text{m}$.

As the pulse propagates through the atmosphere, it induces a magnetization current, which generates a field polarized in both the x- and y-directions. The wave equation for the forward propagating, y-component of the complex field amplitude is $(\partial/\partial\eta + i\Delta k)\,\widehat{E}_y(\eta,\tau) = -i\pi N\mu_m k\,(\widehat{\rho}_{43}(\tau) + \widehat{\rho}_{41}(\tau))$, where the Faraday rotated field is $\widehat{E}_y(\eta,\tau)e^{-i\omega\tau}e^{i\Delta k\eta}\widehat{\mathbf{e}}_y + \text{c.c.}$ The magnetization current is a function of the off-diagonal coherence terms of the density matrix elements $\rho_{43}(\eta,\tau) = \widehat{\rho}_{43}(\tau)e^{-i\omega\tau}e^{i\Delta k\eta}$ and $\rho_{41}(\eta,\tau) = \widehat{\rho}_{41}(\tau)e^{-i\omega\tau}e^{i\Delta k\eta}$. The slowly varying quantities $\widehat{\rho}_{43}(\tau)$ and $\widehat{\rho}_{41}(\tau)$ are given by reduced density matrix equations $(\partial/\partial\tau - i\Delta\omega_{43})\,\widehat{\rho}_{43}(\tau) = i\widehat{\Omega}_{43}(\tau)\rho_0$

and $(\partial/\partial\tau - i\Delta\omega_{41})\,\widehat{\rho}_{41}(\tau) = i\widehat{\Omega}_{41}(\tau)\rho_0$, where $\widehat{\Omega}_{43}(\tau) = \widehat{\Omega}_L(\tau) = -i\mu_m\widehat{E}_0(\tau)/\hbar$, $\widehat{\Omega}_{41}(\tau) = \widehat{\Omega}_R(\tau) = i\mu_m\widehat{E}_0(\tau)/\hbar$, $\rho_0 = \rho_{11} = \rho_{22} = \rho_{33} = 1/3$, $\rho_{44} = 0$, $\Delta\omega_{nm} = \omega - \omega_{nm} + i\gamma_c$, $\omega_{43} = \omega_A - \Omega_0$, $\omega_{41} = \omega_A + \Omega_0$ and it has been assumed that $c\,|\Delta k|\,/\omega \ll 1$.

In the case of conventional Faraday rotation within a long pump duration, $\partial/\partial\tau = 0$, the spatial change in the Faraday rotated field is given by $(\partial/\partial\eta + i\Delta k)\widehat{E}_y(\eta,\tau) = 2\pi kN\mu_m^2(\widehat{E}_0/\hbar)\rho_0\Omega_0/\gamma_c^2$. After propagating a distance L, the ratio between the Faraday rotated and incident intensities is $I_y/I_0 = |E_y|^2/|E_0|^2 = (2\pi)^4(L/\lambda)^2(N\mu_m^2\rho_0/\hbar)^2(\Omega_0/\gamma_c^2)^2$.

In the present model, the pump pulse consists of a pulse train, as shown in Fig. 3.5, in which the duration of the individual pulses, denoted by τ_p, can be comparable or longer than the damping time $1/\gamma_c$. However, the time separation between the pulses T is taken to be long compared to a damping time. With this ordering of timescales, the individual pump pulses excite the density matrix elements ρ_{43} and ρ_{41}, which generate a magnetization current that decays behind the individual pump pulses (Fig. 3.5). The magnetization current is oscillating at the transition frequencies, which are shifted from 762 nm by the Larmor frequency. The frequency shifts lead to a polarization rotation of the magnetization current. This generates a Faraday rotated electric wakefield, co-propagating with and behind each pump pulse.

The general form of the off-diagonal coherence elements is $(\partial/\partial\tau - i\Delta\omega_{nm})\,\widehat{\rho}_{nm}(\tau) = i\widehat{\Omega}_{nm}(\tau)\rho_0$ with solution $\widehat{\rho}_{nm}(\tau) = i\rho_0\int_0^\tau d\tau'\widehat{\Omega}_{nm}(\tau')\exp(-i\Delta\omega_{nm}(\tau' - \tau))$ within the pump pulse. The solution behind the pump pulse is $\widehat{\rho}_{43}(\tau) =$

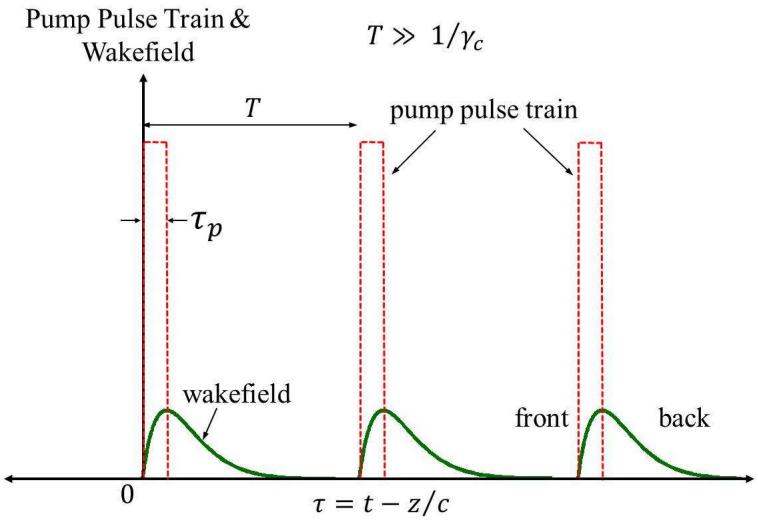

Figure 3.5: Pump pulse train and induced polarization rotated wakefields. The envelopes of both a train of x-polarized laser pulses and the x-component of the induced electric wakefield are shown with dashed-red and solid-green lines, respectively. The wakefield's y-component, the rotated signal, and the magnetization current are not shown for simplicity. The wakefield and magnetization current have a similar polarization and temporal form.

$\widehat{\rho}_{43}(\tau_p)\exp(i\Delta\omega_{43}(\tau-\tau_p))$ and $\widehat{\rho}_{41}(\tau) = \widehat{\rho}_{41}(\tau_p)\exp(i\Delta\omega_{41}(\tau-\tau_p))$. The reduced wave equations for the x- and y-components of the wakefields are

$$(\partial/\partial\eta + i\Delta k)\,\widehat{E}_x(\eta,\tau) = -\,(2\pi/c)\,\widehat{J}_{Mx}(\tau) \tag{3.5a}$$

$$= -C_0 k\rho_0 W_x(\tau)\widehat{E}_0, \tag{3.5b}$$

$$(\partial/\partial\eta + i\Delta k)\,\widehat{E}_y(\eta,\tau) = -\,(2\pi/c)\,\widehat{J}_{My}(\tau) \tag{3.5c}$$

$$= -iC_0 k\rho_0 W_y(\tau)\widehat{E}_0, \tag{3.5d}$$

where $k = \omega/c$, $\omega \gg |\partial/\partial\tau|$, $c\,|\Delta k|$ and $C_0 = 2\pi(N\mu_m^2/\hbar)/\gamma_c \approx 6\times10^{-7}$ is a unitless parameter. In estimating C_0 we have taken the magnetic dipole moment to equal $\mu_m = \mu_e\times10^{-4} = 2.5\times10^{-22}$ statC-cm, the collision frequency to be $\gamma_c = 3.5\times10^9\text{s}^{-1}$

and the O_2 density to be $N = 5.7 \times 10^{18}\,\mathrm{cm}^{-3}$. The current densities are $\widehat{J}_{Mx}(\tau) = (N\mu_m\omega/2)\left(\widehat{\rho}_{43}(\tau) - \widehat{\rho}_{41}(\tau)\right)$ and $\widehat{J}_{My}(\tau) = i(N\mu_m\omega/2)\left(\widehat{\rho}_{43}(\tau) + \widehat{\rho}_{41}(\tau)\right)$. When the collision rate is much larger than the Larmor frequency or detuning $\gamma_c \gg \Omega_0, \omega - \omega_A$, the current densities behind the pulse ($\tau \geq \tau_p$) are given by

$$\widehat{J}_{Mx}(\tau) \approx -\frac{N\mu_m^2 \widehat{E}_0 \rho_0}{\hbar}\frac{\omega}{\gamma_c} W_x(\tau), \tag{3.6a}$$

$$\widehat{J}_{My}(\tau) \approx \frac{N\mu_m^2 \widehat{E}_0 \rho_0}{\hbar}\frac{\omega}{\gamma_c} W_y(\tau), \tag{3.6b}$$

where the time dependence of the wakefield is captured by

$$\begin{aligned} W_x(\tau) &= e^{-\gamma_c(\tau-\tau_p)}\left[\cos\left(\Omega_0(\tau-\tau_p)\right) - e^{-\gamma_c\tau_p}\cos\left(\Omega_0\tau\right)\right. \\ &\quad \left. - \left(\Omega_0/\gamma_c\right)\left(\sin\left(\Omega_0(\tau-\tau_p)\right) - e^{-\gamma_c\tau_p}\sin\left(\Omega_0\tau\right)\right)\right], \end{aligned} \tag{3.7a}$$

$$\begin{aligned} W_y(\tau) &= e^{-\gamma_c(\tau-\tau_p)}\left[\sin\left(\Omega_0(\tau-\tau_p)\right) - e^{-\gamma_c\tau_p}\sin\left(\Omega_0\tau\right)\right. \\ &\quad \left. + \left(\Omega_0/\gamma_c\right)\left(\cos\left(\Omega_0(\tau-\tau_p)\right) - e^{-\gamma_c\tau_p}\cos\left(\Omega_0\tau\right)\right)\right]. \end{aligned} \tag{3.7b}$$

When the laser detuning is larger than the collision rate $\omega - \omega_A \gg \gamma_c$, there is a phase shift from Eqs. (3.6), but, more importantly, the magnitude of the current is suppressed by a factor of $\gamma_c/(\omega - \omega_A)$.

Figure 3.6 shows the wakefield time dependence, Eqs. (3.7), for pump pulse durations of $\tau_p = 0.1$, 0.5, and 1 ns, pump pulse energy of 100 mJ, and spot size of 1 mm. These choices in pulse duration, for a fixed pulse energy, result in a range of pump intensities from $6 \times 10^9\,\mathrm{W/cm}^2$ to $6 \times 10^{10}\,\mathrm{W/cm}^2$. Equations (3.5) indicates that $\widehat{E}_{x,y}/\widehat{E}_0$ is proportional to $W_{x,y}(\tau)$, if Δk is neglected. For the parameters in

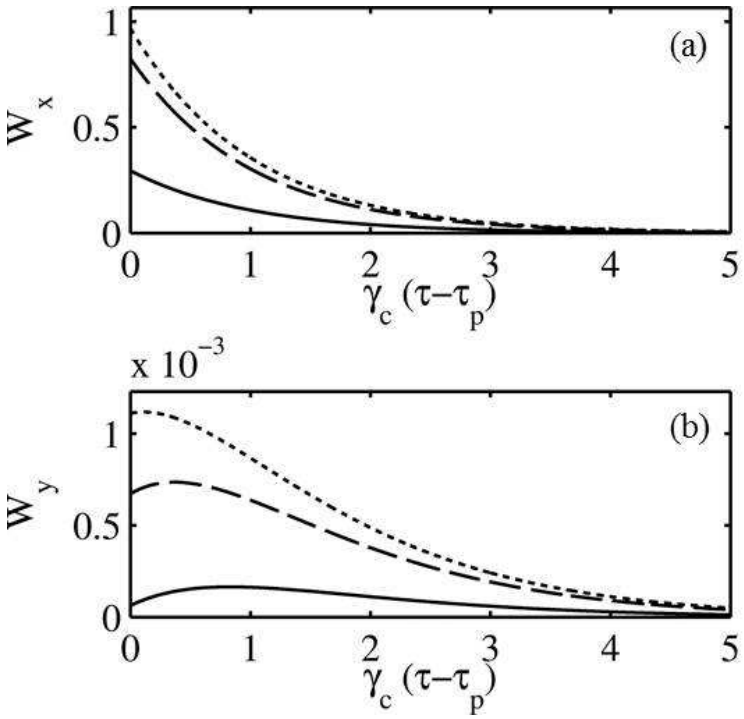

Figure 3.6: (a) x-component and (b) y-components of the wakefield response functions $W_{x,y}(\tau)$, as defined in Eqs. (3.7), behind the pulse for $\Omega_0 = 4.5 \times 10^6$ rad/s. The pulse durations for the solid, dashed, and dotted lines are $\tau_p = 0.1$ ns, 0.5 ns, 1 ns, respectively.

Fig. 3.6, the normalized peak wakefield amplitudes are $|\widehat{E}_x/\widehat{E}_0| \approx 0.5$, 1.5, and 1.6 and $|\widehat{E}_y/\widehat{E}_0| \approx 1 \times 10^{-4}$, 1.2×10^{-3}, and 2×10^{-3}. There is a tradeoff between driving the wakefields with a higher intensity pump ($\widehat{E}_0 \sim \tau_p^{-1/2}$) versus driving it for a longer duration ($W_{x,y} \sim \tau_p$). As a result, for $\tau_p > 3/\gamma_c$, the wakefield amplitude begins monotonically decreasing.

For remote magnetic anomaly detection, small spatial differences in the magnetic field must be measured. Here, we consider measuring the differences in wakefield intensities at two nearby locations (~ 1 m). The locations are referred to as (1) and (2) and have local magnetic fields B_0 and $B_0 + \delta B$. The intensity of the wakefield's y-component at location (1) and (2) is I_1 and I_2, respectively. The fractional change in its intensity of the y-polarized wakefield is $|I_1 - I_2|/I_1 = |\delta I|/I_1 \approx$

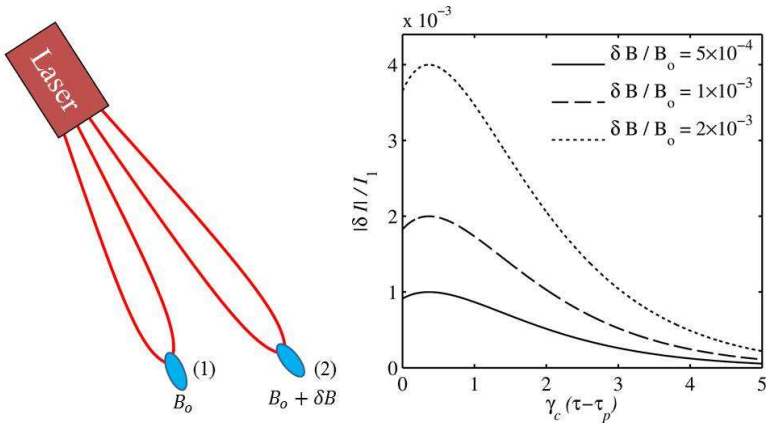

Figure 3.7: Fractional difference in the wakefield intensity for various fractional differences in the magnetic field $\delta B/B_0$. The pump pulse has duration $\tau_p = 0.5\,\text{ns}$, spot size 1 mm, and energy 100 mJ. The differences in magnetic field and corresponding intensities are from two nearby locations.

$2\left|\delta\widehat{E}_y/\widehat{E}_{1y}\right|$, where $\widehat{E}_{1y}$ is the y-component of the wakefield amplitude and $\delta\widehat{E}_y$ is the difference in the wakefield amplitudes between the two locations. Figure 3.7 shows the fractional wakefield intensities for various values of δB. For the values shown, $|\delta I|/I_1 \sim 10^{-3}$.

The pump pulse energy is $I(\pi/2)R^2\tau_p$, where R is the spot size. For a pulse of duration $\tau_p = 0.5\,\text{ns} \approx 2/\gamma_c$, $R = 1\,\text{mm}$ and intensity $I = 10^{10}\,\text{W/cm}^2$, the pump pulse energy is 80 mJ/pulse. For a pulse train, rep-rated at $f_p = 1\,\text{kHz}$, the average pump laser power is $\langle P\rangle = f_p I(\pi/2)R^2\tau_p = 80\,\text{W}$.

It is worth noting that at sufficiently high intensities, the upper level, level $|4\rangle$, can be populated resulting in a laser induced florescence signal to lower energy levels, i.e. levels $|1\rangle$ and $|3\rangle$. This process is known as the Hanle effect and is briefly discussed in Appendix 3.C. The magnetization current resulting from the induced florescence of an x-polarized pump laser is $\mathbf{J}_M \propto e^{-\gamma_c\tau}\cos(\omega_A\tau)\left[\cos(\Omega_0\tau)\widehat{\mathbf{e}}_x - \sin(\Omega_0\tau)\widehat{\mathbf{e}}_y\right]$ [58]. Using polarization filters, the intensity on a detector due to the x- and y-

components of the current density can be measured separately. Taking the ratio of the intensities from the x- and y-components of $\mathbf{J}_M$ gives $I_x/I_y \propto \cot^2(\Omega_0\tau)$. Note that the ratio is independent of the collision rate as long as the individual intensities are greater than the inherent intensity fluctuations.

3.5 Discussion and Concluding Remarks

Remote magnetometry has important applications, such as detection of underwater and underground objects. Detection of the spatial magnetic field fluctuations caused by such an object is important to the US Navy's missions. In the laboratory, under a controlled environment, conventional magnetometry techniques can be used to measure extremely small magnetic field perturbations (pT) [56]. Limitations on remote detection include effects from the laser propagation such as slight variations in the focal intensity due to air turbulence.

Polarized laser light propagating through atmospheric turbulence will develop small fluctuations in polarization. The ratio of the depolarized light intensity to the polarized light intensity is [62] $\langle \Delta I/I \rangle = \pi^{-3/2}\langle \delta n^2 \rangle (L/\ell_0)(\lambda/\ell_0)^2$ where $\langle\ \rangle$ denotes an ensemble average, ΔI is the depolarized intensity, $\langle \delta n^2 \rangle$ is the mean square refractive index fluctuation due to turbulence, L is the propagation range, and ℓ_0 is the inner characteristic scale length associated with the turbulence. As an example, we consider the typical parameters $\lambda = 762\,\mathrm{nm}$, $\ell_0 = 1\mathrm{mm}$, $L = 1\,\mathrm{km}$ and $\langle \delta n^2 \rangle^{1/2} = 10^{-6}$. For these parameters, $\langle \Delta I/I \rangle \approx 10^{-13}$ and depolarization due to turbulence is negligible compared to the polarization rotation of the wakefields.

The paramagnetic species considered here is the oxygen molecule which has an effective magnetic dipole transition ($b^1\Sigma_g^+ - X^3\Sigma_g^-$) near 762 nm. We considered an intense pump laser to induce a polarization rotation of the wakefield. This transition is resonantly driven by a linearly-polarized pump laser pulse. Our examples suggest that the intensity of the rotated component of the wakefield can be measured.

Numerous issues remain to be considered, these include signal detection configuration, i.e. monostatic or bistatic, signal-to-noise ratio limitations, magnetic field orientation relative to the optical axis, and pump laser absorption in the atmosphere.

3.A Transitions in Oxygen Molecule

Oxygen's abundance in the earth's atmosphere, approximately 21% ($N = 5.7 \times 10^{18}\,\mathrm{cm}^{-3}$), and its paramagnetic response make it a possible candidate species for a remote optical magnetometer [22–25]. Molecular oxygen O_2 has two unpaired electrons in the upper level of the ground state, giving it a paramagnetic response. The ground state of oxygen $X^3\Sigma_g^-$, commonly referred to as"triplet oxygen," has total spin $S = 1$ and three degenerate sublevels (see Fig. 3.4). In atmospheric conditions near the surface of the earth (pressure $P = 1\,\mathrm{atm}$, total number density $N_{\mathrm{air}} = 2.7 \times 10^{19}\,\mathrm{cm}^{-3}$, and temperature $T = 23.5\,\mathrm{meV}$), the ground state is fully populated because the next excited electronic state's energy, $E_a = 0.98\,\mathrm{eV}$ is much greater than the thermal energy.

The electronic configuration of molecular oxygen is shown in Fig. 3.8. As seen

in Fig. 3.4, the first excited electronic state of oxygen, $a^1\Delta_g$, is referred to as "singlet oxygen" and only has one spin state $(S, m) = (0, 0)$. This state has an energy of $E_{\mathrm{a-X}} = 0.98\,\mathrm{eV}$, $a^1\Delta_g$ can undergo spontaneous emission via a magnetic dipole transition to the ground state $\mathrm{O}_2(a^1\Delta_g - X^3\Sigma_g^-)$ or $\mathrm{a-X}$. The $\mathrm{a-X}$ transition has a wavelength of $1.27\,\mu\mathrm{m}$. This transition is dominantly due to the orbital angular momentum and has spontaneous emission rate of $A_{\mathrm{a-X}} = 2 \times 10^{-4}\,\mathrm{s}^{-1}$ [63].

The second excited state of oxygen $b^1\Sigma_g^+$ (see Fig. 3.4) will be referred to as the upper state. It is also a spin singlet state with only one sublevel. The upper state can undergo three radiative transitions; $b^1\Sigma_g^+ - X^3\Sigma_g^-(m = \pm 1)$, $b^1\Sigma_g^+ - X^3\Sigma_g^-(m = 0)$, and $b^1\Sigma_g^+ - a^1\Delta_g$, where the first and second transitions are between the different magnetic sublevels of the ground state and are referred to as the A band [59]. The transitions will be referred to as $\mathrm{b-X}, 1$, $\mathrm{b-X}, 0$, and $\mathrm{b-a}$, respectively. The $\mathrm{b-X}$ transitions have an energy of $E_{\mathrm{b-X}} = 1.63\,\mathrm{eV}$, wavelength $\lambda_{\mathrm{b-X}} = 762\,\mathrm{nm}$, and frequency $\omega_{b-X} = 2.5 \times 10^{15}\,\mathrm{rad/s}$. The calculated spontaneous emission rates of the $\mathrm{b-X}, 1$ and $\mathrm{b-X}, 0$ transitions are $A_{\mathrm{b-X},1} = 0.087\,\mathrm{s}^{-1}$ and $A_{\mathrm{b-X},0} = 1.6 \times 10^{-7}\,\mathrm{s}^{-1}$, respectively [63]. The radiation from the $\mathrm{b-X}, 1$ transition can be seen in air-glow, night-glow and aurorae [63]. The $\mathrm{b-X}, 1$ transition is magnetic dipole- and spin-forbidden and it is dominant over the $\mathrm{b-a}$ and $\mathrm{b-X}, 0$ transitions, which are electric quadrupole transitions [59]. This can be explained by a large spin-orbit coupling between the $b^1\Sigma_g^+$ state and the $X^3\Sigma_g^-(m = 0)$ state. The spin-orbit coupling results in a mixing of the levels and the $\mathrm{b-X}, 1$. The $\mathrm{b-a}$ transition has an energy of $E_{\mathrm{b-a}} = 0.65\,\mathrm{eV}$, wavelength $\lambda_{\mathrm{b-a}} = 1.9\,\mu\mathrm{m}$, frequency $\omega_{b-a} = 9.9 \times 10^{14}\,\mathrm{rad/s}$ and spontaneous emission rate of $A_{\mathrm{b-a}} = 1.4 \times 10^{-4}\,\mathrm{s}^{-1}$ [14].

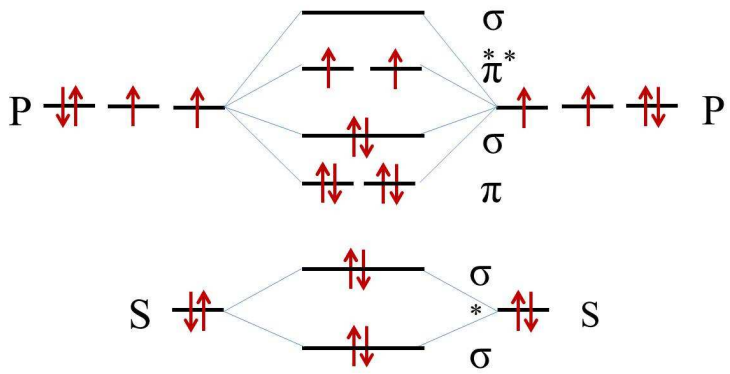

Figure 3.8: Electron occupancy energy levels of O_2 as two oxygen molecules are brought together.

3.B Density Matrix Equations

Interaction of an oxygen molecule with radiation is governed by Schrödinger's equation $i\hbar\partial\left|\psi\right\rangle/\partial t = H\left|\psi\right\rangle$, where $H = H_0 - \boldsymbol{\mu}_m \cdot \mathbf{B}(t)$ is the full Hamiltonian, H_0 is the electronic Hamiltonian after Zeeman splitting, and $-\boldsymbol{\mu}_m \cdot \mathbf{B}(t)$ is the magnetic dipole interaction energy. The state $\left|\psi(t)\right\rangle = \sum_n C_n(t)\left|n\right\rangle$ can be decomposed into the orthogonal energy eigenstates of O_2, $\left|n\right\rangle$. The probability amplitudes $C_n(t)$ are related to the density matrix elements $\rho_{nm}(t) = C_n(t)C_m^*(t)$. The macroscopic electromagnetic fields are driven by a statistical ensemble of molecules, not a single molecule, and therefore it is necessary to use the density matrix equations and to introduce phenomenological relaxations terms, i.e., $\partial\rho_{nm}/\partial t = -i\omega_{nm}\rho_{nm} + i\sum_l\left(\Omega_{nl}\rho_{lm} - \Omega_{lm}\rho_{nl}\right)$ + relaxation terms. The interaction frequency is given by $\hbar\Omega_{nl} = \left\langle n\right|\boldsymbol{\mu}_m \cdot \mathbf{B}(t)\left|l\right\rangle$.

In our model, molecular oxygen is treated as a closed four level atom composed of the ground state $O_2(X^3\Sigma_g^-)$ and the upper level $O_2(b^1\Sigma_g^+)$. The ground state has

three spin sublevels $m = -1,\ 0,\ +1$ which are referred to as states $|1\rangle$, $|2\rangle$, and $|3\rangle$ respectively. The excited upper level is referred to as state $|4\rangle$. The complete set of coupled equations for the density matrix elements, assuming a closed system, are given by

$$\begin{aligned}\partial\rho_{11}/\partial t = \; & -(\Gamma_{12}+\Gamma_{13})\rho_{11} + \Gamma_{21}\rho_{22} + \Gamma_{31}\rho_{33} + \Gamma_{41}\rho_{44} \\ & + i\left(\Omega_{14}\rho_{41} - \Omega_{41}\rho_{14}\right),\end{aligned} \tag{3.8a}$$

$$\partial\rho_{22}/\partial t = \; \Gamma_{12}\rho_{11} - (\Gamma_{21}+\Gamma_{23})\rho_{22} + \Gamma_{32}\rho_{33} + \Gamma_{42}\rho_{44}, \tag{3.8b}$$

$$\begin{aligned}\partial\rho_{33}/\partial t = \; & \Gamma_{13}\rho_{11} + \Gamma_{23}\rho_{22} - (\Gamma_{31}+\Gamma_{32})\rho_{33} + \Gamma_{43}\rho_{44} \\ & + i\left(\Omega_{34}\rho_{43} - \Omega_{43}\rho_{34}\right),\end{aligned} \tag{3.8c}$$

$$\begin{aligned}\partial\rho_{44}/\partial t = \; & -(\Gamma_{41}+\Gamma_{42}+\Gamma_{43})\rho_{44} \\ & + i\left(\Omega_{41}\rho_{14} - \Omega_{14}\rho_{41}\right) + i\left(\Omega_{43}\rho_{34} - \Omega_{34}\rho_{43}\right),\end{aligned} \tag{3.8d}$$

$$\begin{aligned}\partial\rho_{41}/\partial t = \; & -\gamma_{41}\rho_{41} - i\omega_{41}\rho_{41} \\ & + i\Omega_{41}(\rho_{11} - \rho_{44}) + i\Omega_{43}\rho_{31},\end{aligned} \tag{3.8e}$$

$$\begin{aligned}\partial\rho_{43}/\partial t = \; & -\gamma_{43}\rho_{43} - i\omega_{43}\rho_{43} \\ & + i\Omega_{43}(\rho_{33} - \rho_{44}) + i\Omega_{41}\rho_{13},\end{aligned} \tag{3.8f}$$

$$\partial\rho_{13}/\partial t = \; -\gamma_{13}\rho_{13} - i\omega_{13}\rho_{13} + i\Omega_{14}\rho_{43} - i\Omega_{43}\rho_{14}, \tag{3.8g}$$

The population level of state $|n\rangle$ is given by ρ_{nn} while the coherence between the states are given by $\rho_{nm} = \rho^*_{mn}$. The transition frequencies are defined as $\omega_{mn} = \omega_m - \omega_n$, where $\hbar\omega_n$ is energy of the n^{th} state. For example, the state frequencies are $\omega_1 = -\Omega_0$, $\omega_2 = 0$, $\omega_3 = \Omega_0$, and $\omega_4 = \omega_A$, and the transition frequencies are

$\omega_{41} = \omega_A + \Omega_0$, $\omega_{13} = -2\Omega_0$, and $\omega_{43} = \omega_A - \Omega_0$, where ω_A is $O_2(b^1\Sigma_g^+ - X^3\Sigma_g^-)$ transition frequency in the absence of a magnetic field. The Larmor frequency is given by $\Omega_0 = qB_0/(2mc)$, where q is the electric charge, B_0 is the static background magnetic field, and m is the electron's mass. Equations (3.8) imply conservation of population levels, i.e., $\partial(\rho_{11}+\rho_{22}+\rho_{33}+\rho_{44})/\partial t = 0$ (closed system). The populations are additionally normalized unity, i.e., $\mathrm{Tr}(\rho) = 1$. The interaction frequency between states m and state n is $\Omega_{mn} = \Omega_{nm}^*$. Specifically, $\widehat{\Omega}_{43}(z,t) = \mu_m \widehat{B}_L(z,t)/\hbar$ and $\widehat{\Omega}_{41}(z,t) = \mu_m \widehat{B}_R(z,t)/\hbar$, where μ_m is the effective magnetic dipole moment between triplet oxygen and the upper state and $\widehat{B}_{L,R}$ corresponds to is the left (right) handed polarization of the pump field. The rate equation for ρ_{42} is not considered since it does not couple to the those in Eqs. (3.8).

The rates γ_{41} and γ_{43} consist of contributions from (i) elastic collisions (soft, dephasing collisions with no population transfers), (ii) inelastic collisions (population transferring) and spontaneous emission. The elastic collision rate is taken to be the dominate rate and we set $\gamma_{41} = \gamma_{43} = \gamma_{31} = \gamma_c$. In the absence of the pump field and at equilibrium, we have $\rho_{11} = \rho_{22} = \rho_{33} = \rho_0$ and $\rho_{44} = 0$. This implies that $\Gamma_{21} = \Gamma_{12}$, $\Gamma_{31} = \Gamma_{13}$, and $\Gamma_{23} = \Gamma_{32}$ and we take these rates, which include inelastic collisions and spontaneous emission, to equal Γ_0. In addition, the rates Γ_{41}, Γ_{42}, and Γ_{43} consist of inelastic collisions and spontaneous emission and we take these rates to be equal to Γ_U. Taking the inelastic collision rates to be equal, i.e., $\Gamma_0 = \Gamma_U$, the

density matrix equations become

$$\partial\rho_{11}/\partial t = -\gamma_0(\rho_{11} - \rho_{11}^{\rm eq}) + i\left(\Omega_{14}\rho_{41} - \Omega_{41}\rho_{14}\right), \tag{3.9a}$$

$$\partial\rho_{22}/\partial t = -\gamma_0(\rho_{22} - \rho_{22}^{\rm eq}), \tag{3.9b}$$

$$\partial\rho_{33}/\partial t = -\gamma_0(\rho_{33} - \rho_{33}^{\rm eq}) + i\left(\Omega_{34}\rho_{43} - \Omega_{43}\rho_{34}\right), \tag{3.9c}$$

$$\partial\rho_{44}/\partial t = -\gamma_0(\rho_{44} - \rho_{44}^{\rm eq}) + i\left(\Omega_{41}\rho_{14} - \Omega_{14}\rho_{41}\right) + i\left(\Omega_{43}\rho_{34} - \Omega_{34}\rho_{43}\right), \tag{3.9d}$$

$$\partial\rho_{41}/\partial t = -\gamma_c\rho_{41} - i\omega_{41}\rho_{41} + i\Omega_{41}(\rho_{11} - \rho_{44}) + i\Omega_{43}\rho_{31}, \tag{3.9e}$$

$$\partial\rho_{43}/\partial t = -\gamma_c\rho_{43} - i\omega_{43}\rho_{43} + i\Omega_{43}(\rho_{33} - \rho_{44}) + i\Omega_{41}\rho_{13}, \tag{3.9f}$$

$$\partial\rho_{13}/\partial t = -\gamma_c\rho_{13} - i\omega_{13}\rho_{13} + i\Omega_{14}\rho_{43} - i\Omega_{43}\rho_{14}. \tag{3.9g}$$

The phenomenological inelastic damping rate is given by $\gamma_0 = 3\Gamma_0 = 3\Gamma_U \approx 10^8\,\mathrm{s}^{-1}$ [24]. The equilibrium populations for the ground state are $\rho_{11}^{\rm eq} = \rho_{22}^{\rm eq} = \rho_{33}^{\rm eq} = 1/3$ and for the upper state $\rho_{44}^{\rm eq} = 0$.

3.C Resonant Fluorescent Excitation (Hanle effect)

At sufficiently high intensities, laser induced fluorescence, i.e., Hanle effect, can be considered. The Hanle effect refers to the depolarization of resonant fluorescence lines by an external magnetic field [55, 56, 58]. It provides a sensitive experimental technique for a number of measurements, including remote measurement of planetary magnetic fields [64] and spontaneous emission rates [58], and spin depolarization rates [65]. It is also the basis of one of the most sensitive methods for

measuring the lifetime of excited levels of atoms and molecules [66]. In the presence of a magnetic field, the Zeeman sublevels of the ground state are split, resulting in a difference in the resonance frequencies for LHP and RHP light. The resulting phase difference between LHP and RHP light, which is dependent on the ambient magnetic field, alters the polarization of fluorescing radiation.

To discuss this mechanism in more detail, we consider a short intense laser pulse polarized in the x-direction $\mathbf{E}_{\text{pump}} = \widehat{E}_0(\tau)e^{-i\omega_A\tau}(\widehat{\mathbf{e}}_L + \widehat{\mathbf{e}}_R) + \text{c.c.}$ This is just one of many orientations and configurations of the pump polarization and magnetic field direction in which the Hanle effect can occur.

The pump pulse is intense enough to excite level $|4\rangle$ at the expense of levels $|1\rangle$ and $|3\rangle$. The pump pulse duration τ_p is short compared to the collision time which in turn is short compared to a Larmor period. As the short duration, high-intensity polarized pump pulse sweeps by it leaves behind an excited state, which fluoresces with polarization components different then that of the pump. The fluorescence from the excited state ρ_{44} to states ρ_{11} and ρ_{33} is described by the off-diagonal coherence of the molecular density matrix elements $\rho_{43} = -i\widehat{\Omega}_L\tau_p\rho_{44}e^{-i(\omega_{43}-i\gamma_c)\tau}$ and $\rho_{41} = -i\widehat{\Omega}_R\tau_p\rho_{44}e^{-i(\omega_{41}-i\gamma_c)\tau}$, where $\Omega_L = -i\mu_m E_0/\hbar$, $\Omega_R = i\mu_m E_0/\hbar$, $\omega_{43} = \omega_A - \Omega_0$, and $\omega_{41} = \omega_A + \Omega_0$. The magnetization left behind the pump pulse is $\mathbf{M} = -M_0 e^{-\gamma_c\tau}(e^{-i\omega_{43}\tau}\widehat{\mathbf{e}}_L - e^{-i\omega_{41}\tau}\widehat{\mathbf{e}}_R) + \text{c.c.}$ where $M_0 = N\mu_m^2(E_0/\hbar)\tau_p\rho_{44}$. The associated current density is $\mathbf{J}_M = -M_0 e^{-\gamma_c\tau}[\omega_{43}\left\{\cos(\omega_{43}\tau) - i\sin(\omega_{43}\tau)\right\}\widehat{\mathbf{e}}_L + \omega_{41}\left\{\cos(\omega_{41}\tau) - i\sin(\omega_{41}\tau)\right\}\widehat{\mathbf{e}}_R] + \text{c.c.}$, where $\omega_{43}, \omega_{41} \gg \gamma_c$. The current density

has components in the x and y directions [58] which, for $\omega_A \gg \Omega_0$, are given by

$$\mathbf{J}_M = -2M_0 e^{-\gamma_c \tau} \omega_A \cos(\omega_A \tau) \left[\cos(\Omega_0 \tau)\widehat{\mathbf{e}}_x - \sin(\Omega_0 \tau)\widehat{\mathbf{e}}_y\right]. \tag{3.10}$$

By using polarizer filters, the time average intensity on a detector due to the x- and y-components of the current density can be measured separately. Taking the ratio of the intensities from the x- and y-components of $\mathbf{J}_M$ gives $I_x/I_y \propto \cot^2(\Omega_0 \tau)$. The ratio is independent of the collision rate as long as the individual intensities are greater than the inherent intensity fluctuations.

Bibliography

[1] P. Sprangle, E. Esarey, A. Ting, and G. Joyce. Laser wakefield acceleration and relativistic optical guiding. *Applied Physics Letters*, 53(22), 1988.

[2] Ivan P. Christov, Margaret M. Murnane, and Henry C. Kapteyn. High-harmonic generation of attosecond pulses in the "single-cycle" regime. *Phys. Rev. Lett.*, 78:1251–1254, Feb 1997.

[3] S. Tzortzakis, B. Prade, M. Franco, A. Mysyrowicz, S. Hüller, and P. Mora. Femtosecond laser-guided electric discharge in air. *Phys. Rev. E*, 64:057401, Oct 2001.

[4] K. Stelmaszczyk, P. Rohwetter, Guillaume Mejean, Jin Yu, E. Salmon, Jerome Kasparian, Roland Ackermann, J.-P. Wolf, and Ludger Woste. Long-distance remote laser-induced breakdown spectroscopy using filamentation in air. *Applied Physics Letters*, 85(18):3977–3979, Nov 2004.

[5] MS Sherwin, CA Schmuttenmaer, and PH Bucksbaum. Opportunities in THz Science. 2004.

[6] K. Y. Kim. Generation of coherent terahertz radiation in ultrafast laser-gas interactions. *Phys. Plasmas*, 16(5):056706, 2009.

[7] D. H. Auston, K. P. Cheung, J. A. Valdmanis, and D. A. Kleinman. Cherenkov radiation from femtosecond optical pulses in electro-optic media. *Phys. Rev. Lett.*, 53(16):1555–1558, 1984.

[8] L. Xu, X.-C. Zhang, and D. H. Auston. Terahertz beam generation by femtosecond optical pulses in electro-optic materials. *Applied Physics Letters*, 61(15):1784, 1992.

[9] W. Leemans, C. Geddes, J. Faure, Cs. Tóth, J. van Tilborg, C. Schroeder, E. Esarey, G. Fubiani, D. Auerbach, B. Marcelis, M. Carnahan, R. Kaindl, J. Byrd, and M. Martin. Observation of Terahertz Emission from a Laser-Plasma Accelerated Electron Bunch Crossing a Plasma-Vacuum Boundary. *Physical Review Letters*, 91(7):074802, August 2003.

[10] H. Hamster, A. Sullivan, S. Gordon, W. White, and R. Falcone. Subpicosecond, electromagnetic pulses from intense laser-plasma interaction. *Phys. Rev. Lett.*, 71(17):2725–2728, 1993.

[11] D. J. Cook and R. M. Hochstrasser. Intense terahertz pulses by four-wave rectification in air. *Opt. Lett.*, 25(16):1210, 2000.

[12] Markus Kress, Torsten Loffler, Susanne Eden, Mark Thomson, and Hartmut G Roskos. Terahertz-pulse generation by photoionization of air with laser pulses composed of both fundamental and second-harmonic waves. *Opt. Lett.*, 29(10):1120, 2004.

[13] T Bartel, P Gaal, K Reimann, M Woerner, and T Elsaesser. Generation of single-cycle THz transients with high electric-field amplitudes. *Opt. Lett.*, 30(20):2805, 2005.

[14] Xu Xie, Jianming Dai, and X.-C. Zhang. Coherent Control of THz Wave Generation in Ambient Air. *Phys. Rev. Lett.*, 96(7):1–4, 2006.

[15] K. Y. Kim, James H. Glownia, Antoinette J. Taylor, and George Rodriguez. Terahertz emission from ultrafast ionizing air in symmetry-broken laser fields. *Opt. Express*, 15(8):4577, 2007.

[16] Y. S. You, T. I. Oh, and K. Y. Kim. Off-Axis Phase-Matched Terahertz Emission from Two-Color Laser-Induced Plasma Filaments. *Phys. Rev. Lett.*, 109(18):183902, 2012.

[17] Y. S. You, L. A. Johnson, and K. Y. Kim. Conical THz Radiation by Cherenkov Emission in Plasma.

[18] L. A. Johnson, J. P. Palastro, T. M. Antonsen, and K. Y. Kim. THz generation by optical cherenkov emission from ionizing two-color laser pulses. *Phys. Rev. A*, 88:063804, Dec 2013.

[19] C. DAmico, a. Houard, M. Franco, B. Prade, A. Mysyrowicz, a. Couairon, and V. Tikhonchuk. Conical Forward THz Emission from Femtosecond-Laser-Beam Filamentation in Air. *Phys. Rev. Lett.*, 98(23):8–11, 2007.

[20] C D'Amico, A Houard, S Akturk, Y Liu, J Le Bloas, M Franco, B Prade, A Couairon, V T Tikhonchuk, and A Mysyrowicz. Forward THz radiation emission by femtosecond filamentation in gases: theory and experiment. *New J. Phys.*, 10(1):013015, 2008.

[21] Joseph Peñano, Phillip Sprangle, Bahman Hafizi, Daniel Gordon, and Philip Serafim. Terahertz generation in plasmas using two-color laser pulses. *Phys. Rev. E*, 81(2), 2010.

[22] J.P. Davis, M.B. Rankin, L.C. Bobb, C. Giranda, and M.J. Squicciarini. REMAS Source Book. Technical report, Mission and Avionics Tech. Dept., Naval Air Development Center, 1989.

[23] R J Brecha, L M Pedrotti, and D Krause. Magnetic rotation spectroscopy of molecular oxygen with a diode laser. *J. Opt. Soc. Am. B*, 14(8):1921, August 1997.

[24] W. Happer and A.C. Tam. Remote Laser Pumping of Molecular Oxygen In The Atmosphere for Magnetic Field Measurements. Technical report, Columbia Radiation Laboratory, 1977.

[25] Robert J. Brecha. Noninvasive Magnetometry Based on Magnetic Rotation Spectroscopy of Oxygen. *Appl. Opt.*, 37(21):4834, July 1998.

[26] Tobias Kampfrath, Alexander Sell, Gregor Klatt, Alexej Pashkin, Sebastian Mährlein, Thomas Dekorsy, Martin Wolf, Manfred Fiebig, Alfred Leitenstorfer, and Rupert Huber. Coherent terahertz control of antiferromagnetic spin waves. *Nat. Photonics*, 5(1):31–34, 2010.

[27] Sharly Fleischer, Yan Zhou, Robert W. Field, and Keith A. Nelson. Molecular Orientation and Alignment by Intense Single-Cycle THz Pulses. *Phys. Rev. Lett.*, 107(16):163603, 2011.

[28] J. F. Daigle, F Théberge, M Henriksson, T. J. Wang, S Yuan, M Châteauneuf, J Dubois, M Piché, and S. L. Chin. Remote THz generation from two-color filamentation: long distance dependence. *Opt. Express*, 20(6):6825, 2012.

[29] Meihong Lu, Jingling Shen, Ning Li, Yan Zhang, Cunlin Zhang, Laishun Liang, and Xiaoyu Xu. Detection and identification of illicit drugs using terahertz imaging. *J. Appl. Phys.*, 100(10):103104, 2006.

[30] T. I. Oh, Y. S. You, N. Jhajj, E. W. Rosenthal, H. M. Milchberg, and K. Y. Kim. Scaling and saturation of high-power terahertz radiation generation in two-color laser filamentation. *Appl. Phys. Lett.*, 102(20):201113, 2013.

[31] Luc Bergé, Stefan Skupin, Christian Köhler, Ihar Babushkin, and Joachim Herrmann. 3D Numerical Simulations of THz Generation by Two-Color Laser Filaments. *Phys. Rev. Lett.*, 110(7):073901, 2013.

[32] Rongjie Xu, Ya Bai, Liwei Song, Peng Liu, Ruxin Li, and Zhizhan Xu. Initial carrier-envelope phase of few-cycle pulses determined by terahertz emission from air plasma. *Appl. Phys. Lett.*, 103(6):061111, 2013.

[33] Houmei Dai and Jinsong Liu. Phase dependence of the generation of terahertz waves from two-color laser-induced gas plasma. *J. Opt.*, 13(5):055201, 2011.

[34] C Köhler, E. Cabrera-Granado, I Babushkin, L Bergé, J Herrmann, and S Skupin. Directionality of terahertz emission from photoinduced gas plasmas. *Opt. Lett.*, 36(16):3166, 2011.

[35] M. Kolesik and J. V. Moloney. Nonlinear optical pulse propagation simulation: From Maxwells to unidirectional equations. *Phys. Rev. E*, 70(3):036604, 2004.

[36] E. R. Peck and B. N. Khanna. Dispersion of nitrogen. *J. Opt. Soc. Am.*, 56(August):1059, 1966.

[37] Xiaofei Lu and X.-C. Zhang. Generation of Elliptically Polarized Terahertz Waves from Laser-Induced Plasma with Double Helix Electrodes. *Phys. Rev. Lett.*, 108(12):123903, 2012.

[38] J. Wahlstrand, Y.-H. Cheng, and H. M. Milchberg. Absolute measurement of the transient optical nonlinearity in N_2, O_2, N_2O, and Ar. *Phys. Rev. A*, 85(4):043820, 2012.

[39] J. P. Palastro, T. M. Antonsen, and H. M. Milchberg. Compression, spectral broadening, and collimation in multiple, femtosecond pulse filamentation in atmosphere. *Phys. Rev. A*, 86(3):033834, 2012.

[40] P. Sprangle, J. Peñano, B. Hafizi, and C. Kapetanakos. Ultrashort laser pulses and electromagnetic pulse generation in air and on dielectric surfaces. *Phys. Rev. E*, 69(6):066415, 2004.

[41] S. Popruzhenko, V. Mur, V. Popov, and D. Bauer. Strong Field Ionization Rate for Arbitrary Laser Frequencies. *Phys. Rev. Lett.*, 101(19):93003, 2008.

[42] I. Babushkin, W. Kuehn, C. Köhler, S. Skupin, L. Bergé, K. Reimann, M. Woerner, J. Herrmann, and T. Elsaesser. Ultrafast Spatiotemporal Dynamics of Terahertz Generation by Ionizing Two-Color Femtosecond Pulses in Gases. *Phys. Rev. Lett.*, 105(5):053903, 2010.

[43] P. Sprangle, J. Peñano, and B. Hafizi. Propagation of intense short laser pulses in the atmosphere. *Phys. Rev. E*, 66(4):046418, 2002.

[44] George Rodriguez and Georgi L Dakovski. Scaling behavior of ultrafast two-color terahertz generation in plasma gas targets: energy and pressure dependence. *Opt. Express*, 18(14):15130–43, 2010.

[45] V Blank, M D Thomson, and H G Roskos. Spatio-spectral characteristics of ultra-broadband THz emission from two-colour photoexcited gas plasmas and their impact for nonlinear spectroscopy. *New J. Phys.*, 15(7):075023, 2013.

[46] Janos Hebling, Gabor Almasi, Ida Kozma, and Jurgen Kuhl. Velocity matching by pulse front tilting for large area THz-pulse generation. *Opt. Express*, 10(21):1161, October 2002.

[47] L V Keldysh. Ionization in the field of a strong electromagnetic wave. *Sov. Phys. JETP*, 20(5):1307–1314, 1965.

[48] Vladimir S Popov. Tunnel and multiphoton ionization of atoms and ions in a strong laser field (Keldysh theory). *Physics-Uspekhi*, 47(9):855–885, 2004.

[49] A M Perelomov, V S Popov, and M V Terentev. Ionization of atoms in an alternating electric field. *Sov. Phys. JETP*, 23(5):924–934, 1966.

[50] A. Couairon and A. Mysyrowicz. Femtosecond filamentation in transparent media. *Physics Reports*, 441(2-4):47–189, 2007.

[51] S F J Larochelle, A Talebpour, and S L Chin. Coulomb effect in multiphoton ionization of rare-gas atoms. *J. Phys. B*, 31:1215, 1998.

[52] A Talebpour. Semi-empirical model for the rate of tunnel ionization of N2 and O2 molecule in an intense Ti:sapphire laser pulse. *Opt. Commun.*, 163(1-3):29–32, 1999.

[53] I. A. Kotelnikov, A. V. Borodin, and A. P. Shkurinov. Multiphoton ionization of atoms by a two-color laser pulse. *Sov. Phys. JEPT*, 112(6):946–951, 2011.

[54] T. C. Rensink, T. M. Antonsen, J. P. Palastro, and D. F. Gordon. Model for atomic dielectric response in strong, time-dependent laser fields. *Physical Review A*, 89(3):033418, March 2014.

[55] D Budker, W. Gawlik, D.F. Kimball, S.M. Rochester, V.V. Yashchuk, and A Weis. Resonant nonlinear magneto-optical effects in atoms. *Rev. of Mod. Phys.*, 74(4):1153–1201, November 2002.

[56] Dmitry Budker and Derek F. Jackson Kimball. *Optical Magnetometry*. Cambridge University Press, Cambridge, UK, 2013.

[57] G. Bison, R. Wynands, and A. Weis. A laser-pumped magnetometer for the mapping of human cardiomagnetic fields. *Appl. Phys. B: Lasers and Opt.*, 76(3):325–328, March 2003.

[58] Peter W. Milonni and Joseph H. Eberly. *Laser Physics*. John Wiley & Sons, Inc., Hoboken, NJ, USA, March 2010.

[59] Boris Minaev, Olav Vahtras, and Hans Ågren. Magnetic phosphorescence of molecular oxygen. A study of the b1Σg+-X3Σg transition probability using multiconfiguration response theory. *Chem. Phys.*, 208(3):299–311, August 1996.

[60] R.W. Boyd. *Nonlinear Optics*. Elsevier, Burlington MA, 3rd ed. edition, 2008.

[61] Marlan Scully and Suhail Zubairy. *Quantum optics*. Cambridge University Press, Cambridge, 6. printin edition, 2008.

[62] J. W. Strohbehn and S. F. Clifford. *IEEE Trans. Antennas Propagation*, 15(3):416, 1967.

[63] Boris F. Minaev and Hans Å gren. Collision-induced b1Σg+a1 Δg, b1Σg+X3 Σg- and a1ΔgX3Σg - transition probabilities in molecular oxygen. *J. Chem. Soc., Faraday Transactions*, 93(13):2231–2239, 1997.

[64] CK Kumar, L Klein, and M Giraud. Remote measurement of planetary magnetic fields by the Hanle effect. In J. Appleby, editor, *Workshop on Advanced Technologies for Planetary Instruments*, page 14, Fairfax, Virginia, 1993. Lunar and Planetary Institute.

[65] S. Curry, W. Happer, A. Tam, and T. Yabuzaki. Spin Polarization in Flames by Optical Pumping. *Phys. Rev. Lett.*, 40(1):67–70, January 1978.

[66] Alan Corney. *Atomic and Laser Spectroscopy*. Oxford Univ. Press, Oxford, 2006.